Edelweiss Applied Science and Technology
ISSN: 2576-8484
Vol. 9, No. 11, 17-45
2025
Publisher: Learning Gate
DOI: 10.55214/2576-8484.v9i11.10754

Biogenic synthesis of Fe2O3/ZnO bimetallic nanoparticles using fusarium oxysporum extract: Characterisation, optimisation, antimicrobial activity and methyl blue removal

Mohamed Z. Sayed-Ahmed[1,2,3*], Ashraf Elsayed[4], Mai M. Taha[4], Hilal A. Thaibah[1,2], Moaddey Alfarhan[1,2], Aly A. A. Soliman[5], Hesham S. El-Bahkiry[6,7], Reda M. Radwan[7], Elham M. Ali[8]
[1]Pharmacy Practice Research Unit, Department of Clinical Practice, College of Pharmacy, Jazan University, Jazan 45142, Saudi Arabia; mzakaria@jazanu.edu.sa (M.Z.S.A.), hthaibah@jazan.edu.sa (H.A.T.); malfarhan@jazanu.edu.sa (M.A.).
[2]Department of Clinical Practice, College of Pharmacy, Jazan University, Jazan 45142, Saudi Arabia.
[3]Department of Internal Medicine and Infectious Diseases, Faculty of Veterinary Medicine, Mansoura, Egypt; mzakaria@jazanu.edu.sa (M.Z.S.A.).
[4]Department of Botany, Faculty of Science, Mansoura University, Mansoura 35516, University, Mansoura 35516, Egypt; ashraf-badawy@mans.edu.eg (A.E.); maimohsentaha86@gmail.com (M.M.T.)
[5]Department of Physical Sciences, Chemistry Division, College of Science, Jazan University, Jazan 45142, Saudi Arabia; asoliman@jazanu.edu.sa (A.A.A.S.).
[6]Radiation Oncology and Nuclear Medicine Department, Faculty of Medicine, Mansoura University, Mansoura, Egypt.
[7]Department of Diagnostic Radiography Technology, Faculty of Applied Medical Sciences, Jazan University, Jazan 45142, Saudi Arabia; hbahkiry@jazanu.edu.sa (H.S.E.); rradwan@jazanu.edu.sa (R.M.R.).
[8]Department of Aquatic Environment, Faculty of Fish Resources, Suez University, Suez 41522, Egypt; elhamali@narss.sci.eg (E.M.A.).

Abstract: The fungus *Fusarium oxysporum* extract was used to synthesize iron/zinc oxide (Fe_2O_3/ZnO) bimetallic nanoparticles (NPs). To maximize NP yield, a central composite design (CCD) with independent variables, including pH, metal concentration, shaking speed, and incubation duration, was adopted. The greatest yield of the NPs was 1.985 mM at a pH of 7, a metal concentration of 7 mM, an incubation period of 48 hours, and a shaking speed of 140 rpm. These NPs showed potential antimicrobial effectiveness against both gram-positive and gram-negative bacteria. Furthermore, the NPs' activity, which eradicates methyl blue ions, was assessed. The impacts of independent variables (pH, adsorbent concentration, dye concentration, contact time, and shaking speed) were investigated on dye ion biosorption during CCD. The findings indicated that methyl blue concentration, pH, and shaking speed all affected the optimization process. The biosorption of methyl blue ions was modeled using the Langmuir and the Freundlich equilibrium models. The Langmuir model demonstrated a better fit to the experimental data than the Freundlich model. A pseudo-first-order model was used to simulate the methyl blue adsorption process. This study's novel contribution demonstrates the feasibility and effectiveness of using biosynthesized Fe/Zn oxide NPs as adsorbing agents for removing the environmental pollutant methyl blue dye.
Keywords: *Bimetallic nanoparticle, Central composite design, Fusarium oxysporum, Kinetic process, Methyl blue ion.*

1. Introduction

The field of nanotechnology has developed many novel medical techniques and applications using nanoparticles (NPs) [1]. These NPs are typically synthesized using a variety of chemical and physical techniques. Unfortunately, these techniques are time-consuming and expensive and can produce toxic waste that negatively affects the environment and human health. Therefore, innovative and eco-friendly procedures for creating NPs are urgently needed to circumvent such limitations.

History: Received: 19 August 2025; Revised: 26 September 2025; Accepted: 2 October 2025; Published: 28 October 2025
* Correspondence: mzakaria@jazanu.edu.sa

Green chemistry aims to develop chemical and biological processes that reduce waste and the negative environmental impact of existing production methods. One notable modern method in green nanotechnology is substituting harmful compounds with biomaterials [2]. A full range of biological sources provides environmentally friendly precursors for the preparation of small and stable NPs, including plants, bacteria, fungi, yeast, and viruses [3].

The synthesis of NPs using fungi is more effective than using bacteria due to the larger surface area provided by mycorrhizal fungi for the reduction process [4]. Additionally, fungi secrete higher amounts of protein than bacteria, which accelerates the conversion of mineral salts into metal NPs [5]. A novel aspect of this study is that *Fusarium oxysporum* is used as a reducing agent for the production of Fe/Zn bimetallic NPs (BNPs).

BNPs have attracted considerable interest because of their enhanced physical characteristics, including size, shape, and surface morphology. Their distinctive surface properties offer wide application prospects as catalysts and antibacterial agents [6, 7].

Antibacterial agents or antibiotics have broad-spectrum antibacterial capabilities and are used in medical and veterinary applications. They effectively treat and prevent a variety of bacterial infections [8-10]. Chemically produced antibiotics prevent bacterial development and protect living cells from hazardous infections. However, antibiotic efficacy has dramatically declined owing to antibiotic-resistant bacteria, and thus, treatment failure may occur. This problem has motivated the search for novel ways to create antibacterial agents. BNPs made from biological sources have promising applications in several fields, and BNP-based antibacterial drugs have become a major subject of interest [6].

A traditional optimization method involves changing one independent variable while keeping all other variables constant. It is time-consuming and involves a large number of variables. The main drawback is that interactive effects among variables are not included. The response surface methodology has been widely used to optimize biological processes. The central composite design (CCD) model is a main part of response surface methodology. The main advantages of this model are that it is accurate and does not require a three-level factorial experiment to create a second-order quadratic model.

The expansion of industries producing materials, such as dyes, paper, and plastics, which cause pollution, could be toxic to the ecosystem. Dyes are carcinogenic, and their presence in water, even at low concentrations, can cause serious health problems. Ecosystems and aquatic life can be adversely affected by decreased photosynthetic activity and sunlight transmission [11-13].

NPs have an important role in the treatment of textile wastewater. A wide range of dyes and colorants can be effectively decolorized by using a variety of nanomaterials [14-17].

Methyl blue (MB) dye is a water-soluble cationic molecule. It is used as a coloring agent for the paper and textile industries. Adsorption is an effective, versatile, low-cost, highly efficient, and simple method for removing toxic dyes that resist biological degradation. The number of surface groups, high surface area, pore size distribution, thermal stability, ease of regeneration, reusability, disposal, and abundance of the material are all important factors when adsorption is considered in examining a solution [11].

The present work aims to (i) biosynthesize iron oxide/zinc oxide (Fe_2O_3/ZnO) BNPs using the fungal extract of *F. oxysporum*, (ii) characterize the Fe_2O_3/ZnO BNPs through ultraviolet (UV) spectroscopy, Fourier transform infrared (FTIR) spectroscopy, energy-dispersive X-ray (EDX), transmission electron microscopy (TEM), and X-ray diffraction (XRD), (iii) investigate the antimicrobial activity of nanoparticles (NPs) against gram-negative and gram-positive bacteria, (iv) optimize the biosynthesis of Fe_2O_3/ZnO BNPs using central composite design (CCD), (v) optimize methylene blue (MB) eradication through CCD, and (vi) apply equilibrium models and kinetic processes for MB sorption by Fe_2O_3/ZnO BNPs.

2. Materials and Methods

2.1. Biosynthesis of Nanoparticles (NPs) by Fusarium Oxysporum

F. oxysporum was cultivated by growing fungal biomass obtained as agar discs (3–5 discs were used) in a liquid medium of malt glucose yeast peptone medium (MGYP; malt extract, 3 g/L; yeast extract, 3 g/L; peptone, 5 g/L; and glucose, 10 g/L). An MGYP medium (100 mL) was used for each batch, and the biomass was incubated under continuous rotation (130 rpm) for 72 h at 25 ± 1 °C. After the incubation period, the fungal biomass was separated from the media by filtration and washed three times with sterile distilled water to remove media residue. Each 20 g of the fungal biomass extract was immersed in 100 mL of sterile deionized water and incubated under the same conditions for 24 h at an adjusted pH of 6. Ferric chloride and zinc nitrate salts ($FeCl_3$ and $Zn(NO_3)_2{\cdot}6H_2O$) were then added to the medium to a final concentration of 5 mM. The flasks were incubated under the same standard conditions, but placed in the dark to prevent photooxidation of metal ions. The flasks containing cell-free filtrate without metal ions were also incubated under similar conditions to serve as controls. The formed BNPs were obtained from the incubated flasks by drying the biomass at 80 °C, then calcining them at 400 °C for 2 h. As far as we know, using this fungal strain in synthesizing Fe/Zn BNPs has not been reported in the literature.

2.2. Optical Properties of the Synthesised Nanoparticles (NPs)

2.2.1. Ultraviolet–Visible (UV-Vis) Spectroscopy Study

The NPs were characterized using ultraviolet–visible (UV–Vis) absorption spectroscopy with a UV–Vis spectrophotometer (JENWAY-UK) between 200 and 500 nm. The formation of NPs was characterized by the appearance of a new characteristic peak within the 200–500 nm range [18].

2.2.2. X-ray Diffraction Analysis (XRD)

The structural symmetry and structure of the BNPs were observed using an XRD system (D8 ADVANCE, Germany) with Cu-K_a, λ = 1.54 Å, at ambient temperature and in continuous scanning range mode.

2.2.3. Transmission Electron Microscopy (TEM) Analysis

For the detection of the BNPs' shapes and sizes, an NP suspension was dried and dropped on a Gilder G200 TEM grid (standard 200 square mesh, 3.05 mm diameter) and analyzed using JEOL JEM 2100 (HRTEM) operated at a voltage of 200 kV. The crystalline structure of the NPs was examined through selected area electron diffraction (SAED) according to the homogeneity and arrangement of concentric diffraction rings and crystalline planes [19].

2.2.4. Fourier Transform Infrared Spectroscopy (FTIR) Analysis

Functional groups and biomolecules that reduced the metal ions and promoted the formation of BNPs were investigated using an FTIR device (Bruker VERTEX 80, Germany).

2.2.5. Energy-Dispersive X-ray (EDX) Analysis

The presence of elemental iron was confirmed through EDX. EDX microanalysis was carried out with an X-ray micro-analyser (Oxford 6587 INCA) attached to a JEOL JSM-5500 LV scanning electron microscope at 20 kV. The crystal shapes of the BNPs were analysed using Quanta 200 FEG [20].

2.3. Optimisation of Parameters Affecting Nanoparticle (NP) Biosynthesis by Using Central Composite Design (CCD)

To find the optimal conditions for the biosynthesis of NPs, response surface methodology (RSM) was used to gauge the influence of experimental conditions on the yield of the biosynthesis process.

The following conditions were included in the RSM analysis: pH, incubation time (h), vibration (rpm), and metal salt concentration (mM) in the solution.

CCD was used to optimize the four conditions that affect the production of NPs, and the optimal conditions for the biosynthesis of NPs were determined. The four-factor and three-level CCD of 30 trials was conducted, and the correlations among the four variables and NP biosynthesis were studied. Four parameters were investigated at the low level (−1), central level (0), and high level (+1) with $\alpha = 2$ (Table 1). Statistical analysis (ANOVA) for the results was carried out using the Design-Expert 13 software from Stat-Ease [21-24].

Table 1.
Independent variables for the CCD experiment: incubation time, pH, temperature, shaking speed, and salt concentration.

StdOrder	RunOrder	Level	pH	Shaking (rpm)	Salt Conc (mM)	Time (h)
20	1	0	6	130	6	72
19	2	0	6	130	6	72
16	3	1	5	140	5	96
18	4	1	7	140	7	96
12	5	1	7	140	5	48
14	6	1	5	140	7	48
13	7	1	7	120	7	48
11	8	1	5	120	5	48
15	9	1	7	120	5	96
17	10	1	5	120	7	96
22	11	−1	8	130	6	72
30	12	0	6	130	6	72
21	13	−1	4	130	6	72
27	14	−1	6	130	6	24
23	15	−1	6	110	6	72
24	16	−1	6	150	6	72
29	17	0	6	130	6	72
25	18	−1	6	130	4	72
26	19	−1	6	130	8	72
28	20	−1	6	130	6	120
1	21	1	7	120	5	48
10	22	0	6	130	6	72
3	23	1	5	120	7	48
2	24	1	5	140	5	48
6	25	1	7	140	5	96
5	26	1	5	120	5	96
8	27	1	5	140	7	96
4	28	1	7	140	7	48
9	29	0	6	130	6	72
7	30	1	7	120	7	96

2.4. Evaluation of Antimicrobial Activity and Minimum Inhibitory Concentration (MIC) of Bimetallic Nanoparticles (BNPs)

The antimicrobial activity of the biosynthesized nanoparticles (NPs) was investigated against various pathogenic strains. The gram-positive bacterial strains included *Staphylococcus aureus* (ATCC 6538), *Staphylococcus epidermidis* (EMCC number 1353t), *Bacillus cereus* (EMCC number 1080), *Bacillus subtilis* (DMS 1088), and *Streptococcus* sp. The gram-negative bacterial strains used were *Escherichia coli* (ATCC 10536), *Klebsiella pneumoniae* (ATCC 10031), *Enterobacter* sp., and *Salmonella typhi* (ATCC 25566). Additionally, the fungus *Candida albicans* was tested on potato dextrose agar (PDA) media, which consisted of potato infusion, 20 g of dextrose, and 20 g of agar. The agar well diffusion technique was employed for testing. All pathogenic strains were cultured in Luria–Bertani (LB) media, containing 10 g of tryptone, 5 g of yeast extract, 10 g of NaCl, and 20 g of agar. Agar wells with a diameter of 9 mm were punched using a cork borer and filled with different biosynthesized NPs solutions at a concentration of 1 mg/mL. The plates were incubated overnight at 37 °C, and the inhibition zone diameter was measured in millimeters. Double-distilled water served as a negative control, and each experiment was performed in triplicate. The minimum inhibitory concentration (MIC) was determined by testing various concentrations of NPs (0.25, 0.50, 0.75, 1, 2, and 3 mg/mL). The concentration that exhibited approximately 99% inhibition was identified as the MIC value [25, 26].

2.5. Removal Efficacy of the Biosynthesized Bimetallic Fe2O3/ZnO BNPs for Methyl Blue (MB) Dye

The methyl blue (MB) dye was utilized to evaluate the adsorption capacities of the nanoparticles (NPs). Adsorption tests involved mixing 0.1 g of biosynthesized nanoparticles (BNPs) with 100 mL of MB solution at a concentration of 25 ppm in a 250 mL beaker. The pH of the MB solution was adjusted to 7.0 using 0.01 mol L^{-1} HCl or 0.1 mol L^{-1} NaOH, or both, to maintain optimal conditions for adsorption. The study examined the effects of contact time and initial dye concentration on the adsorption capacity. All experiments were conducted in a rotary incubator set at 150 rpm and a temperature of 30°C. The dye concentrations were measured using a UV–Vis spectrophotometer (JENWAY-UK) at 600 nm for MB dye. The adsorption capacity and dye removal efficiency of the biosynthesized NPs were calculated based on standard equations, providing insights into the effectiveness of the nanoparticles in removing MB dye from aqueous solutions.

$$\% R = \frac{(C0 - Ci)}{C0} * 100, \quad (1)$$

$$qe = \frac{(C0 - Ce)}{M} * V, \quad (2)$$

$$qt = \frac{(C0 - Ct)}{M} * V, \quad (3)$$

where *qt* and *qe* (mg/g) are the amounts of dye adsorbed per unit mass of the NPs at time *t* and at equilibrium, respectively; *Co*, *Ct*, and *Ci* (mg/L) are the initial dye concentrations in the solution at time *t* and at equilibrium, respectively; *V* (L) is the volume of dye solution used; and *M* (g) is the mass of the NPs used.

2.6. Biosorption Equilibrium Isotherms and Kinetic Studies

To determine the kinetic mechanism of MB adsorption onto the NPs, we utilized different kinetic models, including pseudo-first-order (Equation 4) [27], pseudo-second-order (Equation 5) [28] and intraparticle diffusion (Equation 6) [29] to fit the experimental data.

$$\text{In } (q_e - q_t) = \text{In } q_e - k_1 t, \quad (4)$$

$$t/q_t = 1/k_2\, q^2_e + t/q_e, \quad (5)$$

$$q_t = k_{int}\, t^{1/2} + C, \quad (6)$$

where q_e (mg/g) is the amount of MB adsorbed at equilibrium, q_t (mg/g) is the amount of MB adsorbed at time *t* (min), and k_1 (min^{-1}), k_2 (mg/g·min), k_{int} (mg/g·$min^{0.5}$), and *C* (mg/g) are the constants related to the boundary layer thickness.

To evaluate the distribution of adsorbate molecules at the solid/liquid interface, we applied some adsorption isotherm models. The obtained equilibrium adsorption data in this work were analyzed using the Langmuir (Equation (7)) [30] and the Freundlich (Equation (8)) [30] models to indicate MB adsorption onto the surfaces of the NPs.

$$C_e/q_e = 1/k_L q_m + C_e/q_m, \quad (7)$$

$$\text{In } q_e = \text{In } K_F + 1/n_F \text{ In } C_e, \quad (8)$$

where q_e (mg/g) is the quantity of MB adsorbed at equilibrium, q_m (mg/g) represents the maximum adsorption capacity for monolayer coverage on the surface of the adsorbent, C_e (mg/L) depicts MB concentration at equilibrium, k_L ($L \cdot mg^{-1}$) is the Langmuir equilibrium adsorption constant, and K_F (mg/g) and n_F are the Freundlich adsorption isotherm constants denoting the adsorption capacity of NPs and the heterogeneity of the adsorption process, respectively.

The influences of different processing factors affecting dye adsorption on NPs, such as initial concentrations of the dye (25, 50, 100, and 250 ppm) and contact time intervals (5–240 min), were optimized.

2.7. Optimisation of Methyl Blue (MB) Removal by Using CCD

Response surface methodology (RSM) was used to investigate the influences of factors such as pH, contact time (h), dye concentration (ppm), and adsorbent concentration (g/L) on the adsorption of dye on the NPs, utilizing CCD with four factors at five levels and five replicates at the center point to fit the data to a second-order polynomial (quadratic) model.

The CCD was utilized to optimize the factors for achieving maximum dye removal from aqueous media by selecting the optimal conditions (Table 2).

Table 2.
Central composite design of MB removal using Fe2O3/ZnO BNPs

Std	Runs	Dye Conc (mM)	Adsorbent Conc (g/L)	pH	Contact Time (h)
14	1	100	2	8	180
19	2	75	1	6	120
1	3	50	2	4	60
9	4	50	2	4	180
27	5	75	3	6	120
16	6	100	4	8	180
10	7	100	2	4	180
23	8	75	3	6	0
12	9	100	4	4	180
5	10	50	2	8	60
18	11	125	3	6	120
24	12	75	3	6	240
6	13	100	2	8	60
8	14	100	4	8	60
22	15	75	3	10	120
25	16	75	3	6	120
17	17	25	3	6	120
13	18	50	2	8	180
3	19	50	4	4	60
2	20	100	2	4	60
20	21	75	5	6	120
21	22	75	3	2	120
11	23	50	4	4	180
15	24	50	4	8	180
7	25	50	4	8	60
26	26	75	3	6	120
4	27	100	4	4	60

3. Results

3.1. Characterization of Biosynthesized Fe2O3/ZnO BNPs

3.1.1. Ultraviolet (UV) Spectroscopy

Fe_2O_3/ZnO BNPs were synthesized through the reduction of metal ions by biomolecules present in the fungal extract. The color of the fungal extract changed from faint pink to dark brown, and this change was the first indicator of the successful synthesis of the NPs. The biosynthesized NPs were then characterized using a UV spectrophotometer in a wavelength range of 200–500 nm. The absorption surface plasmon resonance characteristic peak was observed at 351 nm (Figure 1), whereas no peak appeared in the control fungal extract. This result indicates the stable biosynthesis of the BNPs in the experimental sample.

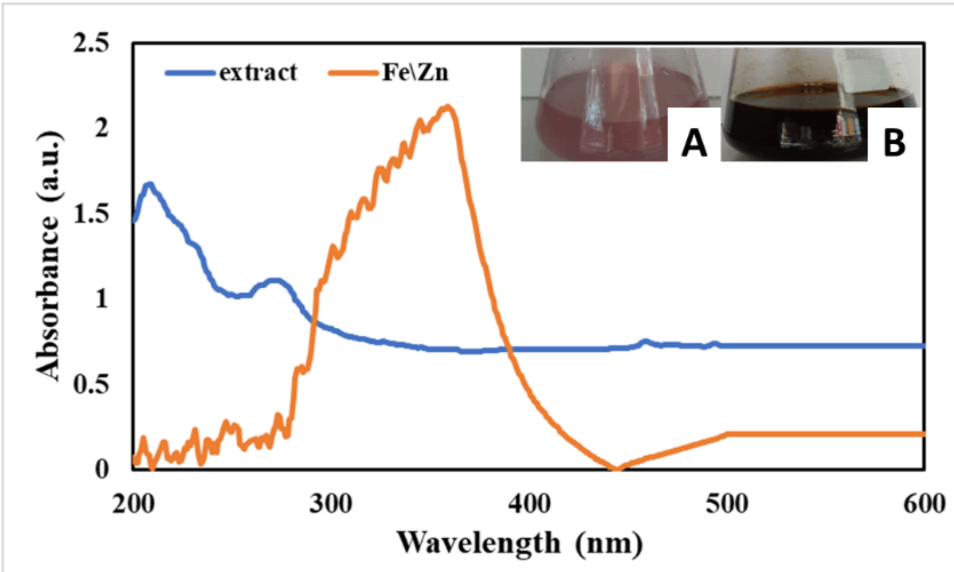

Figure 1.
UV–visible spectra of biosynthesized nanoparticles. (A) Fungal extract, (B) Fe2O3/ZnO BNPs.

3.1.2. FTIR Spectroscopy Analysis

FTIR spectroscopy analysis helps to investigate the functional groups involved in the synthesis of NPs and responsible for the reduction of metal ions and the stability of BNPs compared to the fungal extract control sample (Figure 2). FTIR analysis of Fe_2O_3/ZnO BNPs shows that the band at 3447.04 cm^{-1} relates to the stretching of O-H groups, while the absorption band at 1616.98 cm^{-1} represents the C=C group [31], band at 1046.85 cm^{-1} represent C-O group [32] and 917.02 cm^{-1} represent C-H group. Chemical shifting in absorption peak value towards the lower wavenumber (519 cm^{-1}) indicated the formation of Fe_2O_3/ZnO BNPs.

Edelweiss Applied Science and Technology
ISSN: 2576-8484
Vol. 9, No. 11: 17-45, 2025
DOI: 10.55214/2576-8484.v9i11.10754

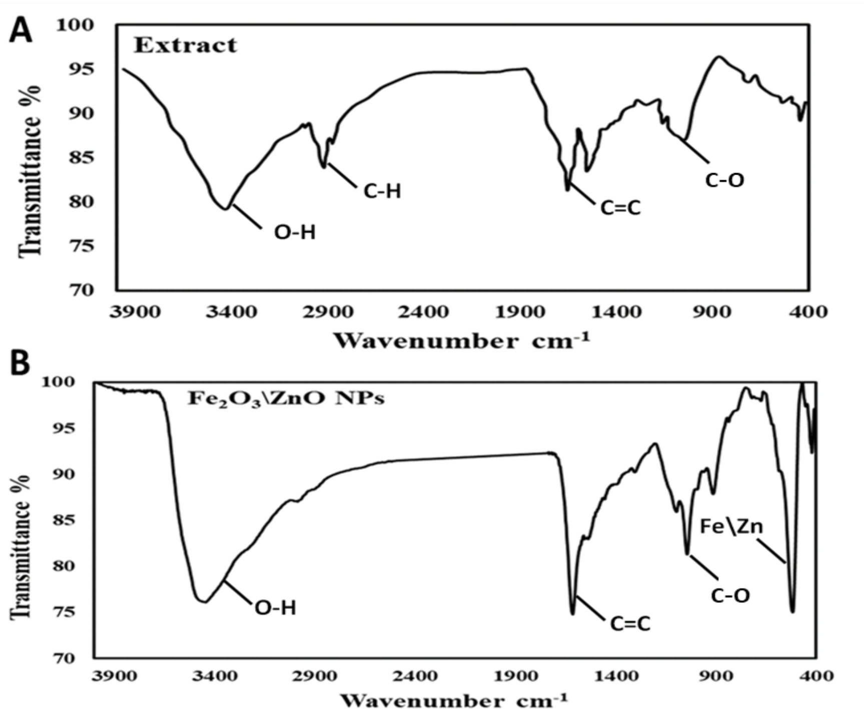

Figure 2.
FTIR spectra of (A) fungal extract and (B) Fe2O3/ZnO BNPs.

3.1.3. X-Ray Diffraction (XRD) Patterns

XRD patterns confirmed the crystalline structures of the biosynthesized NPs. Figure 3 shows the XRD patterns of the biosynthesized Fe_2O_3/ZnO BNPs. The XRD patterns of the Fe_2O_3/ZnO BNPs were compared with the Joint Committee on Powder Diffraction Standards (JCPDS; card No. 01-089-0598) and (card No. 01-089-1397). The 2^{θ} values were detected to confirm the formation of Fe_2O_3/ZnO BNPs. The peaks at 14° and 20° are related to residuals from the fungal extract.

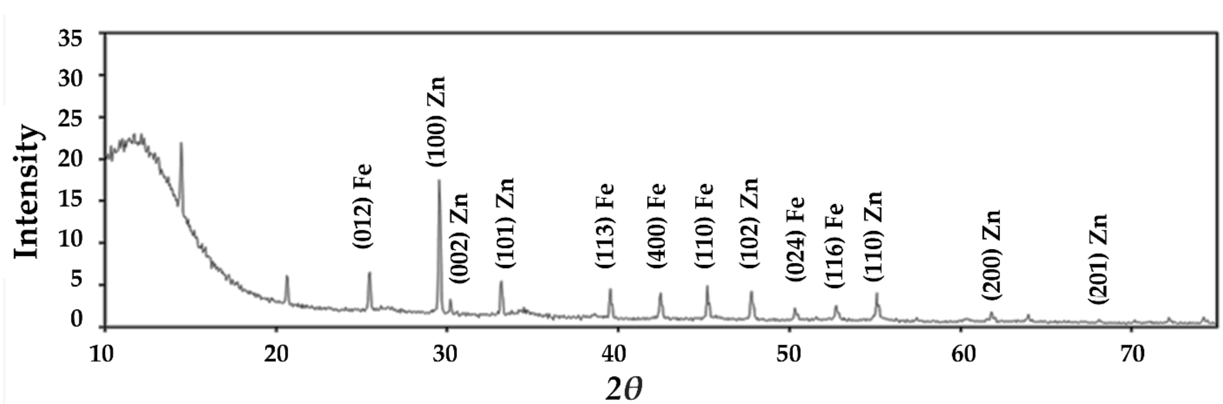

Figure 3.
XRD pattern spectrum of Fe2O3/ZnO BNPs.

3.1.4. Energy-Dispersive X-Ray (EDX) Spectroscopy

The elemental composition of the Fe_2O_3/ZnO BNPs was determined by energy-dispersive X-ray diffraction (XRD). Figure 4 confirms the presence of Fe, Zn, and O elements in the sample's composition.

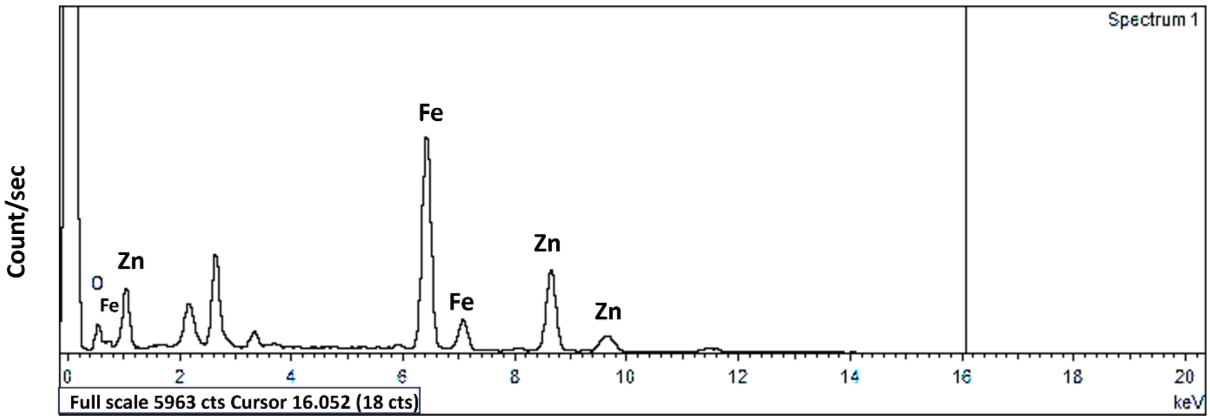

Figure 4.
EDX spectrum of biosynthesized Fe_2O_3/ZnO

3.1.5. Transmission Electron Microscopy (TEM) Analysis

The morphology, crystal structure, and shape of the biosynthesized nanoparticles (NPs) were investigated through transmission electron microscopy (TEM) imaging. The shape, size, and crystal structure of the Fe_2O_3/ZnO biosynthesized nanoparticles (BNPs) are shown in Figure 5. Fe_2O_3/ZnO BNPs are polycrystalline and possess a hexagonal wurtzite crystal structure. The Debye–Scherrer equation was employed to calculate the sizes of the NPs, revealing that the Fe_2O_3/ZnO BNPs ranged from 3 to 13 nm in size, indicating that the diameters of the biosynthesized NPs were less than 20 nm. Selected area electron diffraction (SAED) is an experimental crystallographic technique performed using a transmission electron microscope. It is one of the most widely used techniques for examining two-dimensional electron diffraction patterns. In the SAED pattern, each spot corresponds to a specific diffraction condition. The SAED pattern displayed diffraction rings characteristic of the biosynthesized Fe_2O_3/ZnO BNPs.

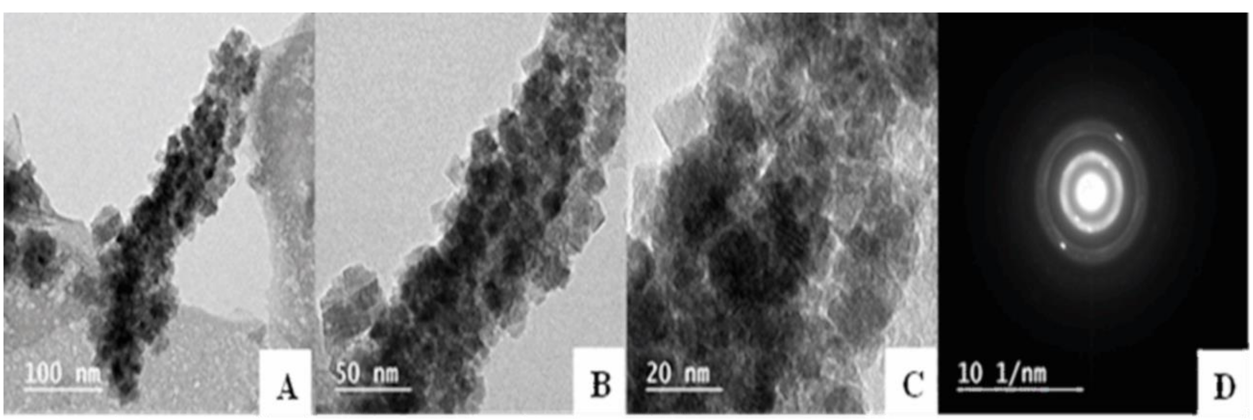

Figure 5.
Electron microscopy of the biosynthesized Fe2O3/ZnO BNPs, (A–C) TEM micrographs and (D) SAED pattern.

DOI: 10.55214/2576-8484.v9i11.10754

3.2. Optimisation of the Biosynthesis of Fe2O3/ZnO BNPs

The biosynthesis of NPs by *F. oxysporum* extract was optimized using CCD. The optimal conditions for Fe_2O_3/ZnO BNPs were obtained at an incubation time of 48 hours, a metal salt concentration of 7 mM, shaking speed of 140 rpm, and pH level of 7 (Table 3).

Table 3.
Maximisation of Fe2O3/ZnO BNPs as responded to independent variables among CCD trials.

Runs	pH	Shaking (rpm)	Salt Conc (mM)	Incubation Time (h)	Fe_2O_3/ZnO BNPs (mM)
1	6	130	6	72	1.627
2	6	130	6	72	1.644
3	5	140	5	96	1.419
4	7	140	7	48	1.985
5	7	140	5	96	1.58
6	5	140	7	48	1.742
7	7	120	7	48	1.92
8	5	120	5	48	1.543
9	7	120	5	96	1.547
10	5	120	7	96	1.799
11	8	130	6	72	1.688
12	6	130	6	72	1.639
13	4	130	6	72	1.285
14	6	130	6	24	1.651
15	6	110	6	72	1.608
16	6	150	6	72	1.696
17	6	130	6	72	1.631
18	6	130	4	72	1.424
19	6	130	8	72	1.889
20	6	130	6	120	1.638
21	7	120	5	48	1.118
22	6	130	6	72	1.687
23	5	120	7	48	1.789
24	5	140	5	48	1.469
25	7	140	5	96	1.528
26	5	120	5	96	1.46
27	5	140	7	96	1.745
28	7	140	7	48	1.95
29	6	130	6	72	1.623
30	7	120	7	96	1.905

Uncertainty for centre points						
N	6	Mean	1.6418	95% CI	0.0188	
Std Dev	0.0234	Std. Error	0.0096	95 CI range	1.6231	1.6606
Uncertainty for all responses						
N	30	Mean	1.6409	95% CI	0.0695	
Std Dev	0.1942	Std. Error	0.0355	95 CI range	1.5715	1.7105

The model F-value (16.21) indicates that the model was significant. There was only a 0.01% chance that an F-value this large would occur due to noise (Table 4).

The *P*-values that were less than 0.05 indicated that the model terms were significant. In this case, A, C, AB, AC, A^2, and A^2C were significant model terms. Values greater than 0.10 indicated that the model terms were not significant.

The lack-of-fit F-value (15.68) indicated that the lack of fit was significant. There was only a 0.33% chance that a lack-of-fit F-value this large would occur due to noise. Significant lack of fit suggested nonlinearity in the data that a quadratic or linear model cannot capture, but the adjusted R-squared of the model performed well for optimization.

Table 4.
ANOVA analysis for the reduced cubic model, which presents the degrees of freedom (Df) of the test.

Source	Sum of Squares	Df	Mean Square	F-Value	*p*-Value
Model	0.9620	9	0.1069	16.21	<0.0001
A-pH	0.0812	1	0.0812	12.32	0.0022
B-Shaking	0.0110	1	0.0110	1.66	0.2119
C-Salt concentration	0.1081	1	0.1081	16.40	0.0006
AB	0.0370	1	0.0370	5.61	0.0281
AC	0.0403	1	0.0403	6.11	0.0225
A^2	0.0321	1	0.0321	4.87	0.0392
B^2	0.0017	1	0.0017	0.2618	0.6145
A^2C	0.0358	1	0.0358	5.43	0.0304
AB^2	0.0228	1	0.0228	3.45	0.0780
Residual	0.1318	20	0.0066		
Lack of Fit	0.1291	15	0.0086	15.68	0.0033
Pure Error	0.0027	5	0.0005		
Cor Total	1.09	29			
Std. Dev.	0.0812		R^2	0.8795	
Mean	1.6400		Adjusted R^2	0.8252	
C.V. %	4.9500		Adeq Precision	14.1501	

Note: Fe/Zn NPs =
$+1.66 + 0.2015*A + 0.0428*B + 0.2325*C$
$+0.1922*AB + 0.2007*AC$
$-0.1343*A^2 + 0.0312*B^2$
$+0.6555*A^2C - 0.5225*AB^2$

Predictions from each fitted linear model were plotted against actual experimental values. The line represents perfect predictions, and the distance of deviation from the line indicates the residual. Predictions for high- and medium-level response values had low residuals and were thus much better than those at low values, which showed more deviations from the line in Figure 6A.

Fitted model predictions were plotted against residual errors (the difference between predicted and actual experimental values). The residual values were normalized by the standard deviation (sigma) for the model in this plot, which provided a visual diagnostic for outlier predictions of the model. Perfect predictions that agree with experimental values have zero residual error, and points close to the zero line represent good predictions (Figure 6B).

As shown in Figure 7, the response surface was maximized for the Fe_2O_3/ZnO biosynthesis response by using the Hill Climbing algorithm, and interaction graphs for the response surface were produced by varying the two factors in the graph and fixing the other two at optimal levels. The interactions among the following factors were explored: A (pH), B (shaking rpm), C (salt concentration), and D (incubation time in minutes).

The response surface was flat in the middle, with three edges exhibiting upward curvature and two edges showing downward curvature, characteristic of a cubic surface. This indicates that once the other two factors are fixed at optimal levels, varying the factors in the AB interaction influences the experiment. The increasing parts of the curve appeared at three settings: high A (>7) plus high B (>120), and low A (<5) plus low/high B (<120 and >140). The downward curvatures occurred at low A/medium B and high A/low B, respectively, indicating decreased response at these set levels.

Edelweiss Applied Science and Technology
ISSN: 2576-8484
Vol. 9, No. 11: 17-45, 2025
DOI: 10.55214/2576-8484.v9i11.10754

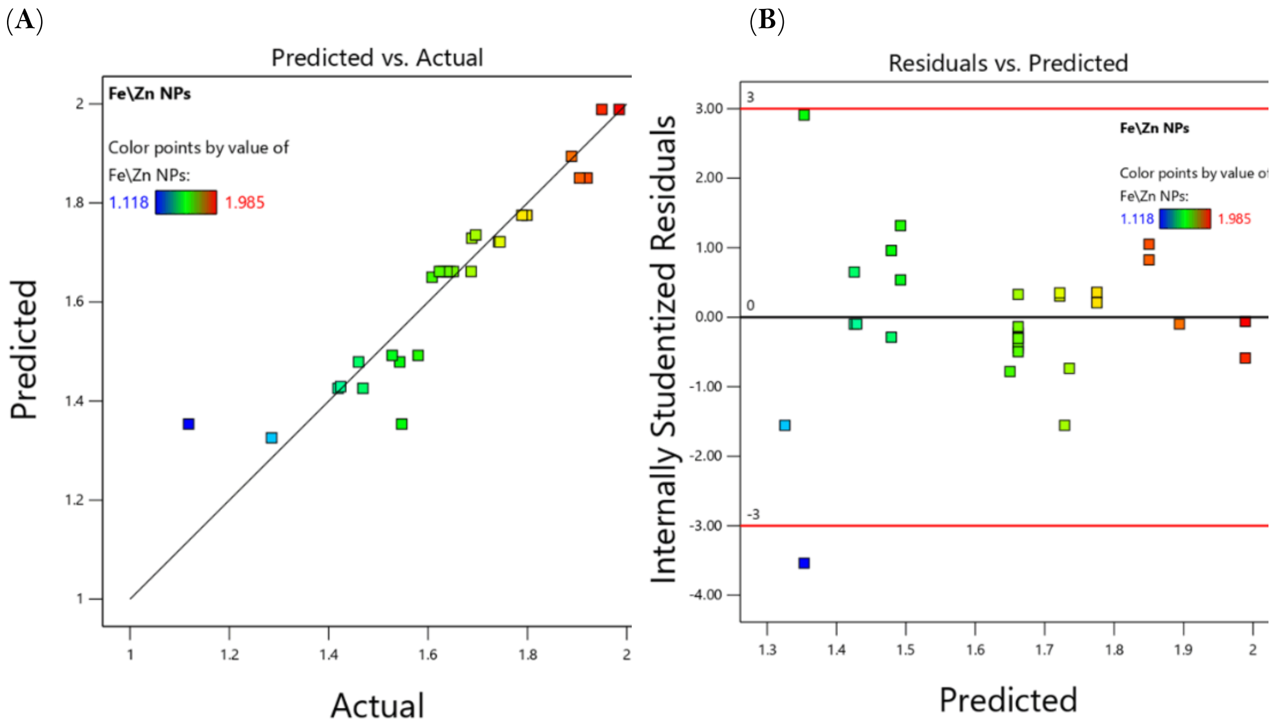

Figure 6.
Fe2O3/ZnO BNP responses: (A) The predicted response values versus the actual response values, (B) standardized residual plots of Fe2O3/ZnO BNPs.

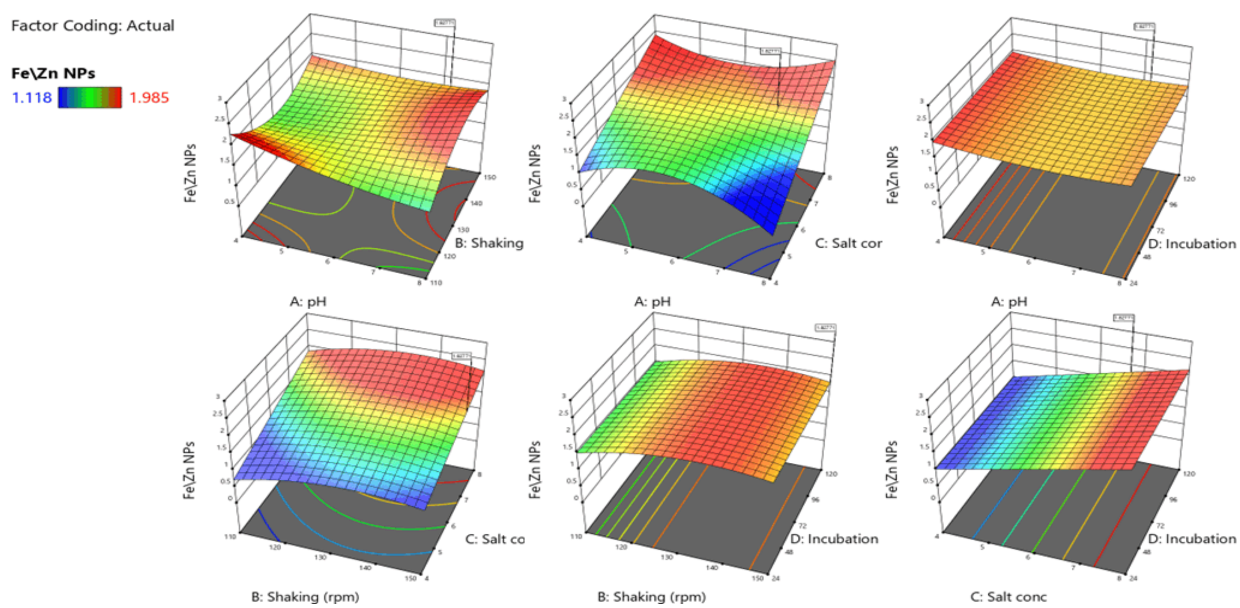

Figure 7.
Three-dimensional surface plot of biosynthesized Fe_2O_3/ZnO BNPs.

CD: The response surface was flat in the middle, with two edges exhibiting upward curvature and two edges showing downward curvature, characteristic of a cubic surface. This indicates that once the other two factors are fixed at optimal levels, varying the factors in the AC interaction has some effect on the experiment. The increasing parts of the curve appeared at two settings: high A (>7) plus high C (>7) and low A (<5) plus high C (>7). The downward curvatures occur at low A/low C and high A/low C, respectively, indicating decreased response at these set levels.

AD: The response surface had some slopes on two sides and some downward curvature in the center, indicating that once the other two factors are fixed at optimal levels, varying the factors in the AD interaction had a significant effect on the experiment. A (pH) had a significant effect on the response, with two settings producing high responses. Low and high settings (<5 and >7) corresponded to the two sloped edges with low middle values. The level sets at each fixed D level were straight, constant lines, indicating the absence of an effect on D once A is fixed.

BC: The response surface exhibited some large slopes with respect to B and a small slope on the edges, with some downward curvature on one edge for C, indicating that once the other two factors are fixed at optimal levels, varying the factors in the BC interaction has a significant effect on the experiment. C (salt concentration) level had a significant effect on response, as C increased with a peak near the 7–8 level, whereas the level sets at each fixed B (shaking) level were slightly curved. Settings around 130, producing high values below or above, had low responses corresponding to downward curvature at the edges.

The response surface exhibited a small slope and slight curvature on one side, indicating that once the other two factors were fixed at optimal levels, varying the factors in the BD interaction has some effect on the experiment. B (shaking) had a significant effect because it moved from low to high levels, thereby increasing the response. The effect leveled off midway beyond 130 (reaching a peak), and the response curve became flat, indicating the absence of an effect beyond that level set. Subsequently, downward curves appeared at high B levels (>140). The level sets at each fixed D level were straight, constant lines, indicating that the level of D was nearly unaffected once B was fixed.

The response surface had some slopes, was almost flat, and had no curvature, indicating that once the other two factors are fixed at optimal levels, varying the factors in the CD interaction has some effect on the experiment. C level had a significant effect on the response. C increased the response, and the level sets at each fixed D level were almost straight, constant lines with no curvature, indicating that the level of D (incubation time) was almost unaffected when C was fixed. High levels of C beyond 7 maximized the response.

3.3. Evaluation of Antimicrobial Activity and Minimum Inhibitory Concentration (MIC) of Fe2O3/ZnO Bimetallic Nanoparticles (BNPs)

The biosynthesized BNPs demonstrated significant activity against tested bacterial pathogens and yeast strains. The maximum inhibition zone diameters at concentrations of 3 mg/mL were 34, 46, 42, 32, 45, 26, 25, 24, 31, and 35 mm against *Bacillus cereus*; *Bacillus subtilis*; *Streptococcus* sp.; *Staphylococcus aureus*; *Staphylococcus epidermidis*; *Escherichia coli*; *Enterobacter* sp.; *Klebsiella pneumoniae*; *Salmonella typhi*; and *Candida albicans*, respectively. The MIC values of the NPs are 3 mg/mL for *Bacillus cereus* and 0.75 mg/mL for *Bacillus subtilis*, *Streptococcus* sp., *Staphylococcus aureus*, and *Staphylococcus epidermidis*. The MIC values for *Escherichia coli*, *Enterobacter* sp., *Klebsiella pneumoniae*, and *Salmonella typhi* are 1 mg/mL, but 2 mg/mL for *Candida albicans* (Table 5 and Figure 8). In general, the Fe_2O_3/ZnO BNPs showed greater potential against gram-positive bacteria than gram-negative bacteria.

Table 5.
Potentiality of different concentrations (mg/mL) of biosynthesized BNPs. against pathogenic bacteria.

Treat.	**Conc. (mg/mL)**	**B.C.**	**B.S.**	**Str.**	**S.A.**	**S.E.**	**E.C.**	**Entro**	**K.P.**	**S.T.**	**C.A.**
Fe/Zn NPs	0.25	6.00 ± 0.12	5.00 ± 0.80	11.00 ± 0.12	14.00 ± 0.16	16.00 ± 0.12	6.00 ± 0.09	5.00 ± 0.60	4.00 ± 0.60	8.00 ± 0.20	16.00 ± 0.10
	0.5	10.00 ± 0.20	21.00 ± 0.14	16.00 ± 0.04	16.00 ± 0.08	19.00 ± 0.03	12.00 ± 0.14	9.00 ± 0.51	8.00 ± 0.57	16.00 ± 0.06	17.00 ± 0.20
	0.75	17.00 ± 0.19	26.00 ± 0.26	21.00 ± 0.14	18.00 ± 0.20	21.00 ± 0.16	15.00 ± 0.16	15.00 ± 0.50	13.00 ± 0.44	18.00 ± 0.08	18.00 ± 0.18
	1	18.00 ± 0.26	31.00 ± 0.37	26.00 ± 0.02	21.00 ± 0.24	26.00 ± 0.20	17.00 ± 0.70	17.00 ± 0.60	15.00 ± 0.04	20.00 ± 0.28	19.00 ± 0.17
	2	26.00 ± 0.24	39.00 ± 0.20	35.00 ± 0.23	27.00 ± 0.40	36.00 ± 0.10	19.00 ± 0.40	19.00 ± 0.44	18.00 ± 0.30	26.00 ± 0.21	27.00 ± 0.16
	3	34.00 ± 0.29	46.00 ± 0.03	42.00 ± 0.09	32.00 ± 0.16	45.00 ± 0.44	26.00 ± 0.64	25.00 ± 0.64	24.00 ± 0.60	31.00 ± 0.13	35.00 ± 0.13
MIC values (mg/mL)		3.00	0.75	0.75	0.75	0.75	1.00	1.00	1.00	1.00	2.00

Note: Treat. Ttreatment; Conc. Concentration; B.C. Bacillus cereus; B.S. Bacillus subtilis; Str. Streptococcus sp.; S.A. Staphylococcus aureus; S.E. Staphylococcus epidermidis; E.C. Escherichia coli; Entro. Enterobacter sp.; K.P. Klebsiella pneumoniae; S.T. Salmonella typhi; C.A. Candida albicans and Candida.

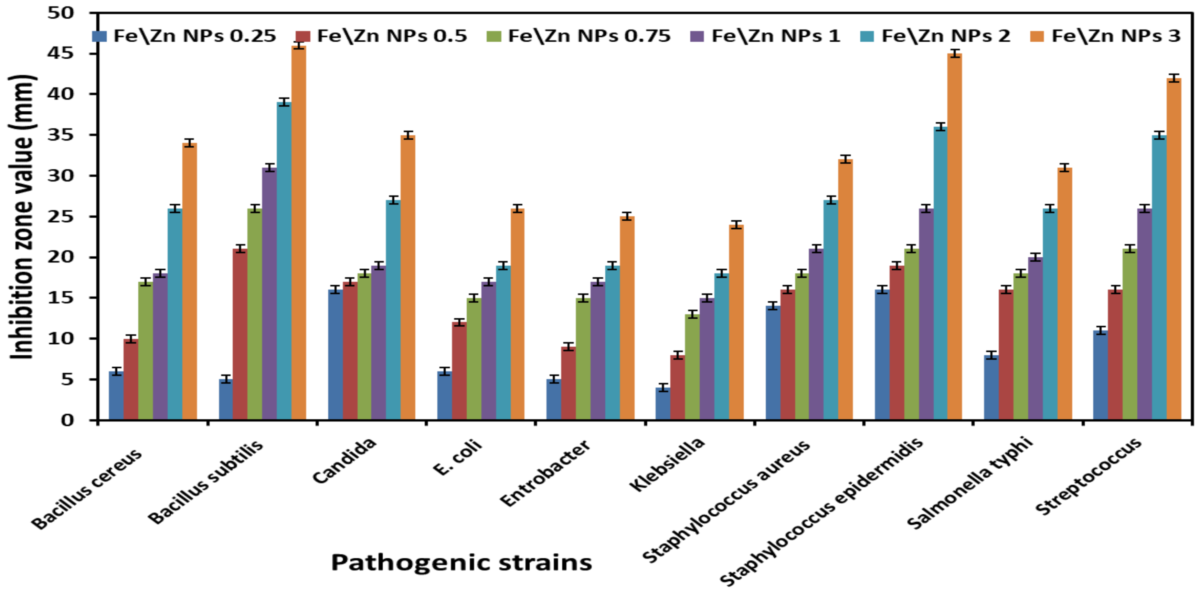

Figure 8.
Antimicrobial activity of Fe2O3/ZnO BNPs.

3.4. Removal Efficacy of Methyl Blue (MB) Dye Using the Biosynthesized Bimetallic Nanoparticles (BNPs)

The dye concentration decreased over time because the dye was adsorbed by the NPs. Figure 9 shows that the absorption peak decreased continuously with increasing exposure time of the NPs with the dye. The adsorption activity of Fe_2O_3/ZnO BNPs increased as the contact time increased because the adsorption activity depended on the surface area, volume, and dispersion of the catalyst in the solution.

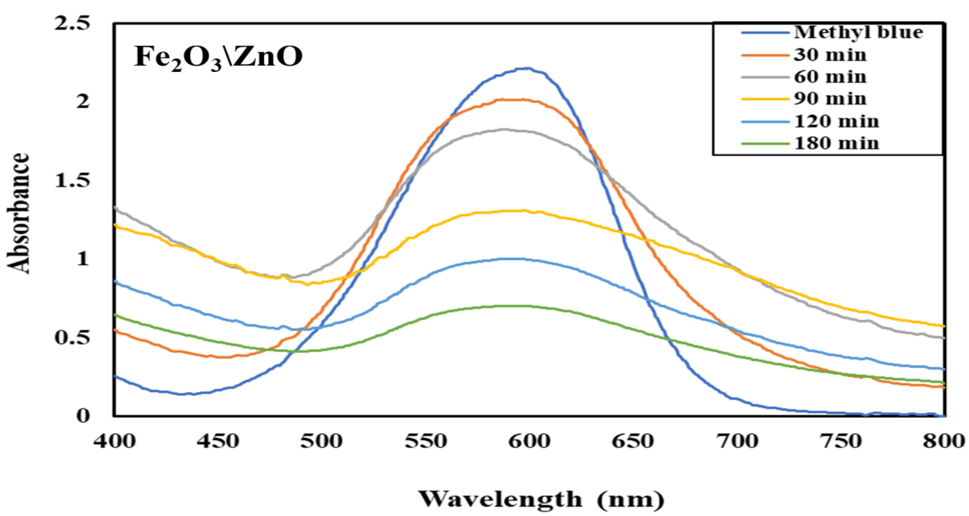

Figure 9.
MB removal using Fe2O3/ZnO BNPs.

3.5. Optimisation of Methyl Blue (MB) Removal Using CCD

From a previous experiment, the adsorption activity of the biosynthesized NPs was examined. The adsorption activity of the NPs increased with time. Based on CCD, 27 rounds of investigation were performed on the variable responses that affected the MB removal rate. Suitable process factors for the adsorption of CR dyes on biosynthesized NPs were obtained using CCD. Compared with fixed optimization techniques, this strategy produced better outcomes while requiring less time and reducing the number of trials needed. By using the complete factorial level of the response surface with three replicates of the centre points for each of the four variables: dye concentration, adsorbent dose, pH, and contact time (Table 6).

Table 6.
Responses of CCD for dye concentration (ppm), adsorbent dosage (g/L), pH, and contact time (min) for MB dye removal.

Std.	Runs	Dye Conc (ppm)	Adsorbent Conc (g/L)	pH	Contact Time (min)	Fe_2O_3/ZnO BNPs (Removal %)
14	1	100	2	8	180	52.55
19	2	75	1	6	120	26.30
1	3	50	2	4	60	81.60
9	4	50	2	4	180	88.25
27	5	75	3	6	120	84.05
16	6	100	4	8	180	86.46
10	7	100	2	4	180	75.79
23	8	75	3	6	0	14.25
12	9	100	4	4	180	81.17
5	10	50	2	8	60	71.34
18	11	125	3	6	120	82.00
24	12	75	3	6	240	86.00
6	13	100	2	8	60	39.45
8	14	100	4	8	60	75.06
22	15	75	3	10	120	87.11
25	16	75	3	6	120	83.80
17	17	25	3	6	120	67.80
13	18	50	2	8	180	82.09
3	19	50	4	4	60	85.73
2	20	100	2	4	60	68.79
20	21	75	5	6	120	12.00
21	22	75	3	2	120	47.00
11	23	50	4	4	180	92.33
15	24	50	4	8	180	73.81
7	25	50	4	8	60	87.12
26	26	75	3	6	120	84.25
4	27	100	4	4	60	58.58
Uncertainty for center points						
N	3	Mean	84.03	95% CI	0.26	
Std Dev	0.23	Std Error	0.13	95 CI range	83.78	84.29
Uncertainty for all responses						
N	27	Mean	69.43	95% CI	8.65	
Std Dev	22.94	Std Error	4.42	95 CI range	60.78	78.09

Model selection was performed using backward feature selection based on a *p*-value threshold close to the significance level ($\alpha = 0.1$). Starting with a quadratic model that includes all the linear and interaction terms, the model was refined iteratively by removing the least significant term and refitted until no term was above the desired threshold. The final selected model, which is a reduced quadratic model, is illustrated in Table 7.

Table 7.
ANOVA for the reduced quadratic model (R % Fe2O3/ZnO BNPs).df represents the degree of freedom of the test.

Source	Sum of Squares	df	Mean Square	F-Value	*p*-Value
Model	6232.79	4	1558.20	4.6000	0.0075
B-Adsorbent Conc	111.73	1	111.73	0.3299	0.5716
D-Contact time	1807.12	1	1807.12	5.3400	0.0307
B^2	4154.24	1	4154.24	12.2700	0.0020
D^2	638.71	1	638.71	1.8900	0.1835
Residual	7451.25	22	338.69		
Lack of Fit	7451.15	20	372.56	7329.00	0.0001
Pure Error	0.1017	2	0.0508		
Cor Total	13,684.05	26			
Fit Statistics					
Std. Dev.	18.40		R^2	0.4555	
Mean	69.43		Adjusted R^2	0.3565	
C.V. %	26.51		Adeq Precision	6.9788	

Note: Final Model Equation R % Fe/Zn NPs = + 85.20 + 2.16*B + 8.68*D − 12.74*B2 − 4.99*D2.

The model as a whole had a *p*-value that was significant at $\alpha = 0.05$ level and even at the 0.01 level, showing strong performance. Only D and B^2 quadratic terms were significant at $\alpha = 0.05$, and all the other terms were not significant.

The lack of fit was significant, indicating that the model did not fit many data points, possibly because excessive noise in the measurements exerted considerable nonlinear effects on the data or because of a large number of outliers. The model provided adequate adjusted R^2 performance and was thus used in the overall response surface optimization.

The adequate precision model measured the signal-to-noise ratio. A ratio greater than 4 is desirable. The current ratio indicates an adequate signal, and this model can be used to navigate the design space.

Terms with high model coefficients in the model equation had a larger effect than terms with low coefficients and indicated whether the response increases or decreases. A negative coefficient decreased the response when it increased, and a positive coefficient increased the response when it increased. B^2 has the highest coefficient, followed by D.

Table 8 is the residual table containing the predictions obtained using the fitted model equation for each data point. The values were compared with the actual experimental values. The difference between them was used to obtain the residual (error) for the model.

Table 8.
Residual table for (R% Fe2O3/ZnO BNPs).

Run Order	Actual Value	Predicted Value	Residual	Standard Order
1	52.55	73.98	−21.44	14
2	26.30	29.93	−3.63	19
3	81.60	56.63	24.97	1
4	88.25	73.98	14.27	9
5	84.05	85.20	−1.15	27
6	86.46	78.30	8.16	16
7	75.79	73.98	1.81	10
8	14.25	47.86	−33.61	23
9	81.17	78.30	2.87	12
10	71.34	56.63	14.72	5
11	82.00	85.20	−3.20	18
12	86.00	82.57	3.43	24
13	39.45	56.63	−17.17	6
14	75.06	60.94	14.12	8
15	87.11	85.20	1.91	22
16	83.80	85.20	−1.40	25
17	67.80	85.20	−17.40	17
18	82.09	73.98	8.11	13
19	85.73	60.94	24.79	3
20	68.79	56.63	12.16	2
21	12.00	38.56	−26.56	20
22	47.00	85.20	−38.20	21
23	92.33	78.30	14.03	11
24	73.81	78.30	−4.49	15
25	87.12	60.94	26.18	7
26	84.25	85.20	−0.9459	26
27	58.58	60.94	−2.36	4

Figure 10 shows the predictions from the fitted linear model plotted against actual experimental values. The line represents perfect predictions, and the deviations from the line represent the residuals. Predictions for high response values have low residuals and are therefore more accurate than those at low values, which have greater deviations from the line.

Edelweiss Applied Science and Technology
ISSN: 2576-8484
Vol. 9, No. 11: 17-45, 2025
DOI: 10.55214/2576-8484.v9i11.10754

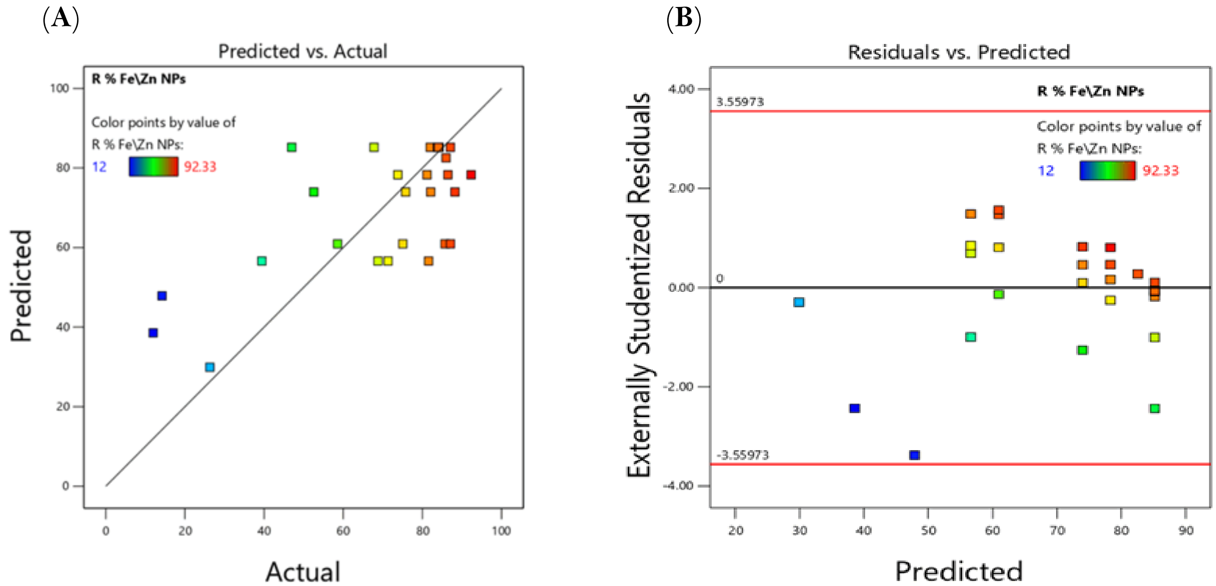

Figure 10.
Model evaluation of MB removal by Fe_2O_3/ZnO BNPs: (A) The predicted response values versus the actual response values; (B) Standardized residual plots.

Figure 11 shows the fitted model predictions versus residual errors (differences from actual experimental values). The residual value is normalized by the standard deviation (sigma) of all residuals for each model. This provides a visual diagnostic for outlier predictions in the model. Perfect predictions have zero residual error, and points closer to the zero line represent better predictions.

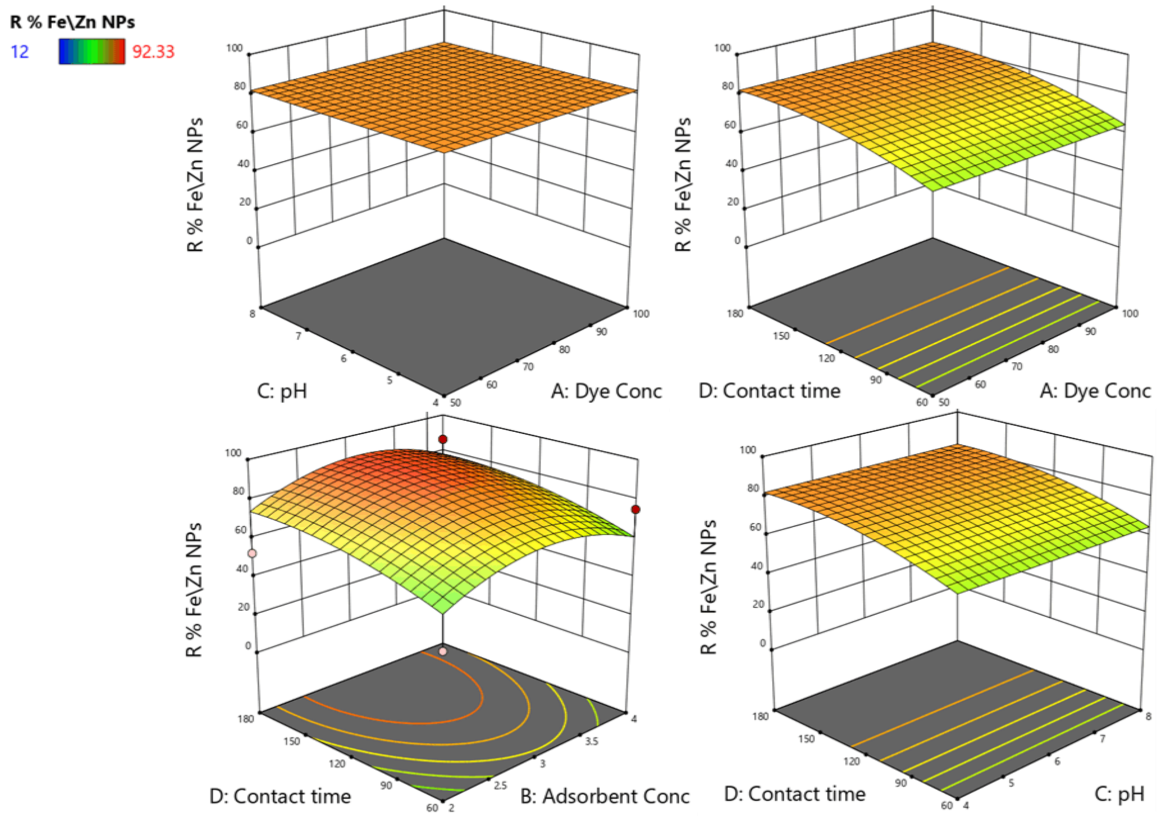

Figure 11.
Three-dimensional surface plots of MB removal using Fe_2O_3/ZnO BNPs.

The response surface was maximized with respect to the Fe_2O_3/ZnO absorption response by using a Hill Climbing algorithm, and interaction graphs for the response surface were produced by varying the two factors in the graph and fixing the other two at optimal levels (Figure 11).

AC: The response surface had an extremely small slope and was flat with no curvature, indicating that once the other two factors are fixed at optimal levels, varying the factors in the AC interaction has a small or no effect on the experiment. A (dye) had a small or no effect on the response, as A increased the response slightly, and the level sets at each fixed A level were straight, constant lines, indicating that the level of C (pH) was nearly unaffected.

The response surface had a small slope and a slight curvature on one side, indicating that once the other two factors are fixed at optimal levels, varying the factors in the AD interaction has some effect on the experiment. D^2 had a large effect as it moved from low levels to high levels and increased the response, and then the effect leveled off midway beyond 120 (reaching a peak), and the response curve became flat, indicating that the level set was not affected. The level sets at each fixed D level were straight, constant lines, indicating that the level of A (dye) was nearly unaffected when D was fixed.

BD: The response surface had a hill-shaped peak with a large slope and curvature that can be climbed from multiple sides of the curve, indicating that once the other two factors are fixed at optimal levels, varying the factors in the BD interaction has a significant effect on the experiment. The peak of the hill surface occurred at a B (adsorbent) level of 3 and D^2 (contact time) level of 120. The level sets were curved ovals on the contour, indicating that varying B and D have a significant effect on the response. As B increased to 3, the response increased, and the values approached the center of the oval and then dropped off to the edge beyond that. The effect of D approached the center, as D increased to 120 and then dropped to the edge of the oval beyond that level.

The response surface has a small slope and exhibits slight curvature on one side, indicating that once the other two factors are fixed at optimal levels, varying the factors in the CD interaction has a minimal effect on the experiment. D^2 (contact time) had a significant effect; as it increased from low to high levels, the response also increased. Beyond 120, the response curve leveled off, becoming flat, which indicates the absence of an effect beyond that level. The level sets at each fixed D level were straight, constant lines, suggesting that the level of C (pH) was nearly unaffected when D was fixed.

3.6. Effect of Contact Time

We studied the effect of contact time on dye removal by biosynthesized NPs to explore the equilibrium time for dye removal. Adsorption efficiency was measured with different contact times from 5 min to 300 min (Figure 12). The calculation of the removal percentage of MB indicated that the maximum adsorption of MB in the presence of biosynthesized Fe_2O_3/ZnO was 84%. The MB dye removal by BNPs increased with contact time from 5 min to 240 min. The increase in dye adsorption may be due to a large number of active sites available on the surfaces of NPs for dye adsorption. As contact time further increased, the adsorption of the dye decreased, likely because of the saturation of the adsorbent surface and the repulsive force between the dye molecules on the surface of the adsorbent [33-35].

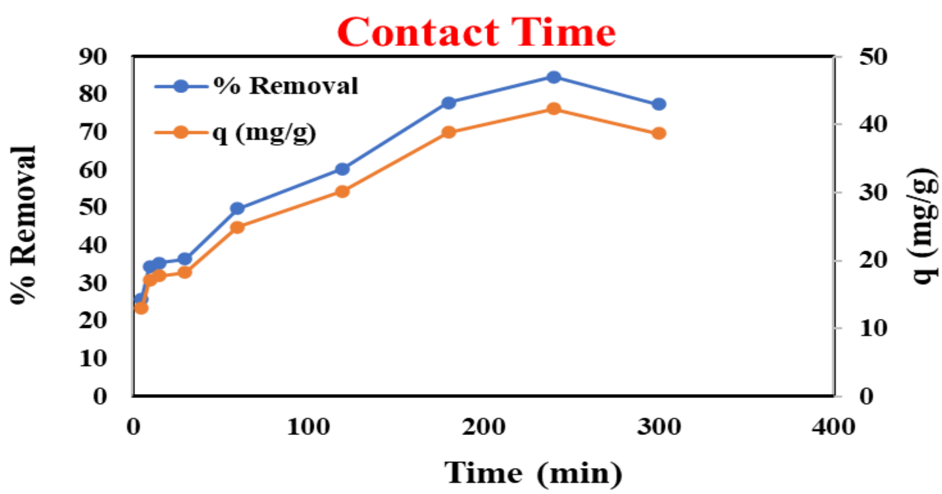

Figure 12.
Contact time of MB removal by BNPs.

3.7. Effect of Initial Dye Concentration

At dye concentrations of 25, 50, 100, and 250 ppm, Figure 15 examined the impact of starting dye concentration on the removal of MB dyes (Figure 13). The other aspects of the experiment remained unchanged. The elimination of MB dye was inversely correlated with dye concentration. The adsorption efficiency of NPs was 97.9% for MB dye at a low dye concentration (25 ppm). This pattern of dye removal might be caused by the surfaces of NPs having numerous active sites available for dye adsorption at low starting dye concentrations. However, as the dye concentration increased, fewer surface-active binding sites were available because the dye saturated the binding sites [36].

Edelweiss Applied Science and Technology
ISSN: 2576-8484
Vol. 9, No. 11: 17-45, 2025
DOI: 10.55214/2576-8484.v9i11.10754

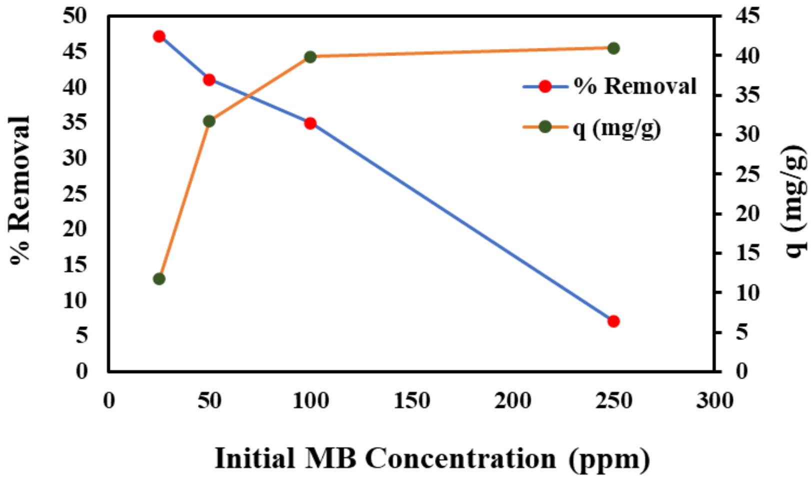

Figure 13.
Plot of removal % and q (mg/g) vs. initial CR concentration of BNPs.

3.8. Biosorption Kinetic Studies

The kinetic study relied on the removal rate of the dye from the aqueous phase by the biosorbent based on varying contact times. Investigations were conducted to determine how different time intervals (5–240 min) of contact between the biosorbent and dye affected the NP's ability to adsorb MB dye (100 mL of 50 mg/L). This factor is extremely important in the study of kinetic isotherms. The kinetic properties of MB adsorption by the NPs have been investigated by fitting the data on the effect of contact time to several kinetic models, namely, pseudo-first order, pseudo-second order, and intraparticle diffusion models. Figure 14 shows that as the contact time increased, the removal efficiency also increased. This relationship was clearly demonstrated in the graph when contact time was increased from 5 min to 60 min, leading to a proportional increase in the biosorption capacity (q) of the NPs. This effect can be attributed to the presence of available active sites and functional groups on the NPs' surface. These groups saturated and decreased the biosorption rate. In this study, the experimental data were fitted to pseudo-second-order models. The results aligned with findings from previous studies. Table 9 shows the different kinetic parameters and R^2 values for each model. Figure 16 illustrates the plot of the intraparticle diffusion kinetic model for MB adsorption on the BNPs. The inclusion of several linear regions in the plot suggests that the MB adsorption process involved multiple steps. Initially, the dyes diffused into the adsorbent particles. Subsequently, dye molecules entered macropores through diffusion. Finally, equilibrium was reached after molecules diffused into the inner layers and micropores.

Table 9.
Parameters obtained from different kinetic models for the adsorption of MB onto the biosynthesized Fe_2O_3/ZnO BNPs.

Kinetic Model		Fe_2O_3/ZnO
Pseudo-First-Order	q_e (mg/g) Calculated	34.709
	q_e (mg/g) Experimental	42.383
	k_1 (min^{-1})	−0.013
	R^2	0.949
Pseudo-Second-Order	q_e (mg/g) Calculated	44.837
	q_e (mg/g) Experimental	42.383
	k_2 (g/mg min)	0.001
	R^2	0.981

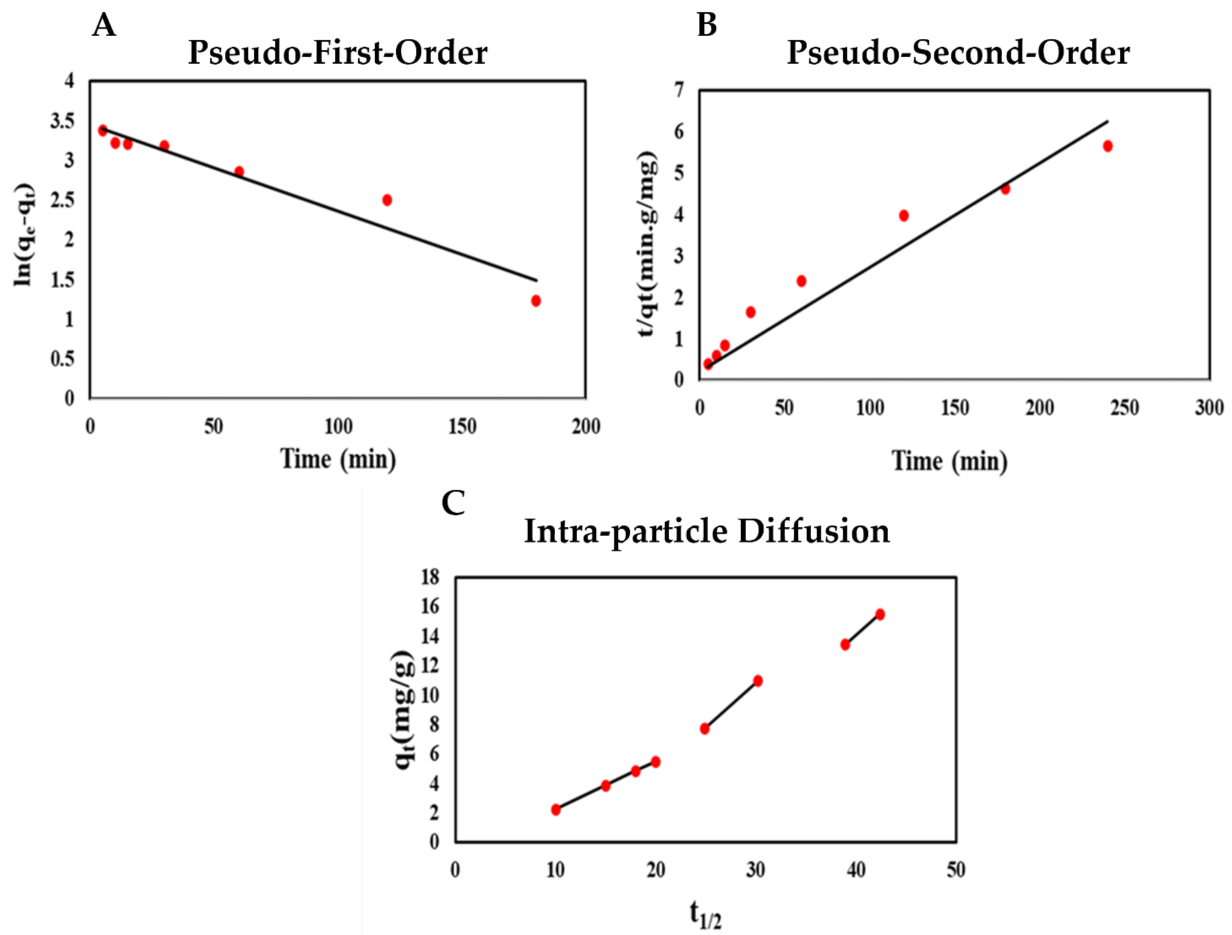

Figure 14.
Different kinetic models for biosorption of MB onto the biosynthesized Fe_2O_3/ZnO BNPs: (A) first-order plots, (B) second-order plots, and (C) intraparticle diffusion plots.

3.9. Biosorption Equilibrium Isotherms

The biosorption isotherm is typically used to illustrate the distribution of dye molecules between liquid and solid phases at equilibrium. Experimental data were fitted to various commonly used isotherm models to identify the most appropriate model for describing the process. The data were fitted to the

Langmuir and the Freundlich isotherms. The models, their constants, and biosorption parameters are presented in Figure 15 and Table 10. The R^2 values of the linearized plots indicated that the Langmuir equation provided a better fit to the experimental data than the Freundlich equation. This suggests a monolayer biosorption process with homogeneous biosorption sites and similar biosorption capacities, assuming a constant biosorption energy. The RL value for MB dye removal was 0.228, which falls between 0 and 1, indicating favorable biosorption. In contrast, the Freundlich model assumes multilayer biosorption with heterogeneous site energies. A low correlation coefficient for its linearized plot was observed, implying that the Freundlich model is less suitable for modeling the biosorption process.

Table 10.
Kinetic parameters of different equilibrium models for the adsorption of MB onto the biosynthesized Fe2O3/ZnO BNPs.

Equilibrium Model		**Fe_2O_3/ZnO**
Freundlich	K_F (mg1⁻ ¹/n L1/n g⁻¹)	839.056
	n_f	18.81
	R^2	0.125
Langmuir	q_e (mg/g) Calculated	17.455
	K_L (L mg⁻¹)	−0.098
	R^2	0.987

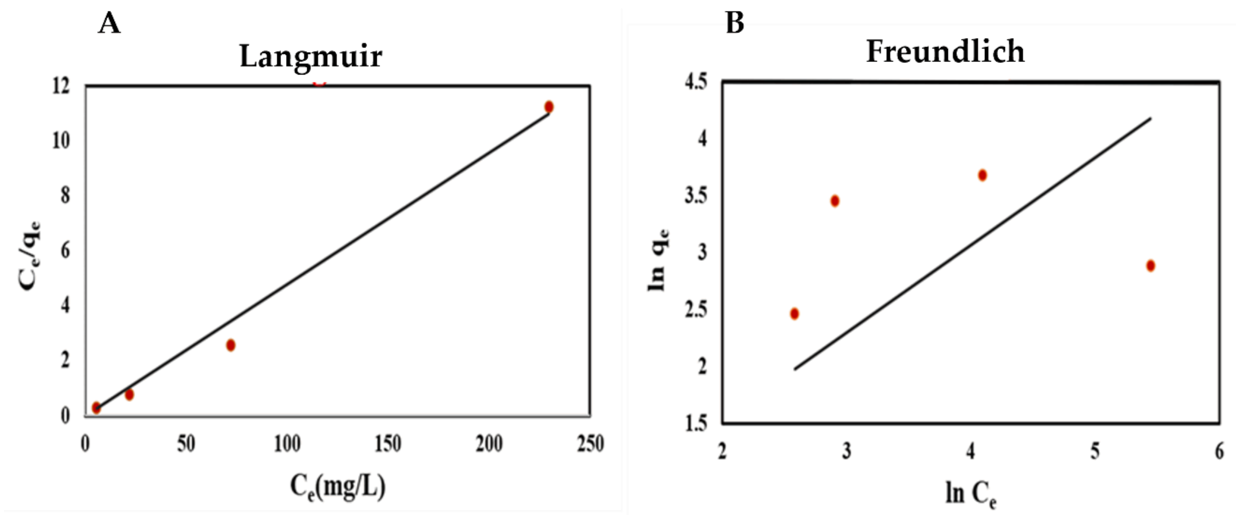

Figure 15.
Plots of (**A**) Langmuir and (**B**) Freundlich isotherms for the biosorption of MB onto the biosynthesized NPs.

4. Discussion

In the present work, *F. oxysporum* was used for the biosynthesis of Fe_2O_3/ZnO BNPs. The color of the cell-free extract changed from faint pink to dark brown. To confirm the composition and synthesis of the nanoparticles, some optical analyses were performed. The first type of spectroscopic analysis conducted was UV–vis spectroscopy. In this study, the characteristic peak of Fe_2O_3/ZnO BNPs was observed at 351 nm. In the UV–Vis spectra of ZnO nanoparticles, the absorption peak ranges from 360 to 380 nm [37]. The shift in the absorption peak was indicated by bimetallic Fe_2O_3/ZnO nanostructure formation [38, 39].

FTIR analysis indicates the fungal metabolites responsible for the bioreduction of NPs. According to FTIR analysis, the protein in the extract may have significantly affected the stability of the Fe_2O_3/ZnO BNPs. The polycrystalline structures of the NPs were investigated using XRD patterns. Fe_2O_3 NPs exhibited rhombohedral structures, confirmed by peaks at 2θ values of 24.02°, 35.4°, 40.6°, 49.2°, and 54.09°, corresponding to the (012), (110), (113), (024), and (116) planes, respectively. These peaks were consistent with JCPDS card No. 0598-089-01 [40, 41]. The peaks of ZnO NPs were compared with JCPDS card No 01-089-1397 and indicated that ZnO NPs had hexagonal crystalline structures, which were confirmed by the peaks at 2θ values of 31.3°, 33.9°, 35.7°, 47.9°, 56.07°, 62.2°, and 67.6°, assigned to the (1 00), (0 02), (1 0 1), (02 1), (110), (00 2), and (01 2) planes, respectively [42, 43]. We used the SAED image to confirm the polycrystalline structures of the Fe_2O_3/ZnO BNPs (Figure 5D).

The EDX spectrum of Fe_2O_3/ZnO BNPs provided the elemental composition of the Fe_2O_3/ZnO BNPs. EDX showed peaks identified as iron, zinc, and oxygen and indicated that NPs formed as nanooxides.

The shapes and morphology of the NPs were investigated through TEM. The NPs' size depends on the composition and the nature of the medium used [44]. The sizes of the Fe_2O_3/ZnO BNPs ranged from 3 nm to 13 nm. The variations in the shapes and sizes of the NPs were due to the contribution of several reducing and capping agents acting during the biological synthesis. Chemical methods can produce NPs with uniform shapes and sizes because of differences in the chemicals used as stabilizing and reducing agents [45, 46].

Design of Experiment (DoE) analysis tests all variables and their interactions through efficient sampling of the design space, which can be used to develop models of the factor and response space without testing all possible interactions. CCD is a type of DoE analysis used for optimization and was employed in this study.

The optimization of biological production utilizes different statistical approaches to identify and optimize parameters that significantly affect the process and predict the interactions between factors. Optimization of these factors that influence the synthesis of BNPs is the initial step in the process. CCD was used to study the effect of various variables, such as incubation time, pH, shaking speed, and metal salt concentration on the production of NPs [23]. Thirty different trials were selected and performed to obtain samples about the optimal factors that maximize the responses. ANOVA was used to test the significance of the factors in the biosynthesis of Fe_2O_3/ZnO BNPs. According to the results of ANOVA, the reduced cubic model with high-order interactions between pH and salt concentration is the best model for the biosynthesis of the Fe_2O_3/ZnO BNPs. Model terms with *p*-values less than 0.05 were statistically significant. The significant model terms included A (pH) and C (salt), and the interaction terms included AB (pH-shaking), AC (pH-salt), A^2 (high-order pH interaction), and A^2C (high-order pH and salt interaction). *p*-values greater than 0.05 indicated that the model terms were not significant. The ANOVA results indicate that the overall model (all terms considered together) was statistically significant with a p-value <0.0001. The F-value of the overall model was 16.21, which reflected the significance of the model. For Fe_2O_3/ZnO BNPs, the optimal conditions were found at run number 2, where pH, shaking speed, salt concentration, and incubation time were 6, 130 rpm, 6 mM, and 72 hours, respectively.

The NPs demonstrated excellent antimicrobial activity against most of the tested pathogenic strains. The inhibitory effect of NPs can be related to DNA structural disintegration or disruption of enzyme activity induced by the generation of highly reactive oxygen species that damage the cell membrane and cell wall [47-49].

The NPs demonstrated an excellent inhibitory effect against all tested pathogenic microbes and exerted greater effects on gram-positive bacteria than on gram-negative bacteria.

The effect of initial dye concentration on the removal of MB dyes was studied according to changes in dye concentration. At low dye concentrations (25 ppm), the adsorption efficiency of NPs was 92% for MB dye. This pattern of dye removal may be due to low initial dye concentrations and a large number of active sites on the surfaces of NPs for dye adsorption. However, as dye concentration increased, the number of surface-active binding sites decreased because of the saturation of the binding sites by the dye molecules [36].

Adsorption kinetics is a fundamental aspect of adsorption system design because it provides information about the rate and time of adsorption. Kinetics play an essential role in characterizing the adsorption dynamics of an adsorbate and can provide important information about possible adsorption mechanisms. In this study, the kinetics of MB adsorption on the NPs were investigated by fitting the contact-time effect data to kinetic models, namely, pseudo-first-order and pseudo-second-order models. The removal of MB dyes fitted well with the pseudo-second-order kinetic model.

The pseudo-first-order kinetic model describes the adsorption process in solid and liquid systems, assuming that two measurable factors are proportional to the number of free active sites: (i) the ratio of the rate of adsorption to the change in adsorption capacity at a given point in time, and (ii) the equilibrium and percentage occupancy of adsorption sites [50, 51]. In this form, the physical process is dominant because of the weak interaction between the adsorbent and the adsorbent surface.

The pseudo-second-order kinetic model assumes that chemisorption is the main process, and the adsorption rate is related to the square of the number of free active sites [52, 53]. In this study, the kinetic studies were fitted to a pseudo-second-order model with an R^2 of 0.9981. The relationship between the amounts of dyes, such as MB, adsorbed on the BNPs, and the dye concentration at equilibrium can be described by adsorption isotherms [54, 55]. The adsorption performance and the ability of the adsorbent to adsorb dyes from aqueous solutions were analyzed using isotherm models. To determine the most suitable isotherm model for representing MB dye adsorption onto the NPs, the Langmuir and the Freundlich models were employed in data analysis.

An experimental Freundlich isotherm describes multilayer adsorption on a heterogeneous surface [30, 56]. The Langmuir model assumes that (i) all adsorption sites are equal, (ii) each site can hold only one adsorbate molecule, and (iii) all sites do not depend strongly on the adsorbed amount of an adsorbate [57-59]. In this study, the results fitted more closely to the Langmuir isotherm model, with an R^2 of 0.987 for MB.

The optimal conditions for MB removal using BNPs were investigated. CCD was used to optimize different factors affecting MB removal by NPs. ANOVA was employed to examine the significance of three types of variables. A reduced quadratic model was fitted to the data, and the ANOVA of the model yielded an F value of 4.6, indicating that the overall model was significant. The p-value was 0.0075, which was less than the significance threshold (0.05), signifying that the overall model (considering all model terms) was significant. Another parameter for evaluating the model's quality is the coefficient of determination (R^2) and adjusted R^2. The R^2 and adjusted R^2 values for the MB removal model were 0.4555 and 0.3565, respectively. The lower value of adjusted R^2 compared to R^2 indicates that the model did not overfit. The optimal conditions for MB removal were as follows: a concentration of 50 ppm, an adsorbent dosage of 4 g/L, a pH of 4, and a contact time of 180 minutes, with a maximum removal rate of 92%.

5. Conclusions

Our novel contributions include the use of a *Fusarium oxysporum* fungal strain to produce Fe/Zn bimetallic nanoparticles (BNPs) and the application of these nanoparticles to remove methylene blue (MB) dye, which differs chemically from other dyes and pollutants. The nanoparticles demonstrated significant antibacterial properties against both gram-positive and gram-negative bacteria, with a high inhibition zone observed against *Bacillus subtilis*. Additionally, potent antibacterial activity was noted against *Bacillus cereus*, *Bacillus subtilis*, *Streptococcus* sp., *Staphylococcus aureus*, and *Staphylococcus epidermidis*. The initial dye concentration inversely affected the removal efficiency of MB dye, as higher dye concentrations led to decreased adsorption due to saturation of the nanoparticle binding sites. Kinetic and equilibrium isotherm studies were conducted for MB dye removal using Fe_2O_3/ZnO BNPs. The kinetic data fitted well to the pseudo-second-order model with an R^2 value of 0.981, and the intraparticle diffusion model indicated that the adsorption process occurred in three stages. The equilibrium data conformed to the Langmuir isotherm model with an R^2 of 0.987. The maximum removal efficiency of MB dye by Fe_2O_3/ZnO BNPs was 92%. During the central composite design (CCD), the F value was 4.6, and the p-value was 0.0075. The nanoparticles exhibited excellent antibacterial properties and proved effective as adsorbents for removing MB dye from aqueous media. In conclusion, our findings suggest that these nanoparticles have promising applications in wastewater treatment as antimicrobial agents, owing to their bio-friendly and eco-friendly properties.

Transparency:

The authors confirm that the manuscript is an honest, accurate, and transparent account of the study; that no vital features of the study have been omitted; and that any discrepancies from the study as planned have been explained. This study followed all ethical practices during writing.

Copyright:

References

[1] M. M. Hulikere and C. G. Joshi, "Characterization, antioxidant and antimicrobial activity of silver nanoparticles synthesized using marine endophytic fungus-Cladosporium cladosporioides," *Process Biochemistry*, vol. **82**, pp. 199-204, 2019. https://doi.org/10.1016/j.procbio.2019.04.011

[2] A. Michna, M. Morga, Z. Adamczyk, and K. Kubiak, "Monolayers of silver nanoparticles obtained by green synthesis on macrocation modified substrates," *Materials Chemistry Physics*, vol. 227, pp. 224-235, 2019. https://doi.org/10.1016/j.matchemphys.2019.01.072

[3] M. Jamzad and M. Kamari Bidkorpeh, "Green synthesis of iron oxide nanoparticles by the aqueous extract of Laurus nobilis L. leaves and evaluation of the antimicrobial activity," *Journal of Nanostructure in Chemistry*, vol. 10, pp. 193-201, 2020. https://doi.org/10.1007/s40097-020-00341-1

[4] A. Elsayed, G. M. El-Shamy, and A. A. Attia, "Biosynthesis, characterization, and assessment of zirconia nanoparticles by fusarium oxysporum species as potential novel antimicrobial and cytotoxic agents," *Egyptian Journal of Botany*, vol. 62, no. 2, pp. 507-522, 2022. https://doi.org/10.21608/ejbo.2022.114070.1869

[5] A. G. Rodrigues *et al.*, "Functional textiles impregnated with biogenic silver nanoparticles from Bionectria ochroleuca and its antimicrobial activity," *Biomedical Microdevices*, vol. 21, p. 56, 2019. https://doi.org/10.1007/s10544-019-0410-0

[6] S. K. Bhanja *et al.*, "Green synthesis of Ag@ Au bimetallic composite nanoparticles using a polysaccharide extracted from Ramaria botrytis mushroom and performance in catalytic reduction of 4-nitrophenol and antioxidant, antibacterial activity," *Environmental Nanotechnology, Monitoring & Management*, vol. 14, p. 100341, 2020. https://doi.org/10.1016/j.enmm.2020.100341

[7] X. Jiang, X. Fan, W. Xu, R. Zhang, and G. Wu, "Biosynthesis of bimetallic Au–Ag nanoparticles using Escherichia coli and its biomedical applications," *ACS Biomaterials Science & Engineering*, vol. 6, no. 1, pp. 680-689, 2019. https://doi.org/10.1021/acsbiomaterials.9b01297

[8] S. Elmogy *et al.*, "Biological insights of fluoroaryl-2, 2′-bichalcophene compounds on multi-drug resistant staphylococcus aureus," *Molecules*, vol. 26, no. 1, p. 139, 2020. https://doi.org/10.3390/molecules26010139

[9] A. Elsayed, A. Mohamedin, T. Ata, and N. Ghazala, "Molecular characterization of multidrug resistant clinical Escherichia coli isolates," *American Biochemistry and Molecular Biology*, vol. 6, pp. 72-83, 2016.

[10] N. Naimi-Shamel, P. Pourali, and S. Dolatabadi, "Green synthesis of gold nanoparticles using Fusarium oxysporum and antibacterial activity of its tetracycline conjugant," *Journal de mycologie medicale*, vol. 29, no. 1, pp. 7-13, 2019. https://doi.org/10.1016/j.mycmed.2019.01.005

[11] A. Blanco-Flores, H. P. Toledo-Jaldin, A. R. Vilchis-Néstor, G. López-Téllez, V. Sánchez-Mendieta, and D. M. Ávila-Márquez, "Metallurgical slag properties as a support material for bimetallic nanoparticles and their use in the removal of malachite green dye," *Advanced Powder Technology*, vol. 31, no. 7, pp. 2853-2865, 2020. https://doi.org/10.1016/j.apt.2020.05.012

[12] D. G. Nkosinathi, B. K. Albertus, S. S. Jabulani, M. Siboniso Siphephelo, and R. V. Pullabhotla, "Biosynthesis, characterization, and application of iron nanoparticles: In dye removal and as antimicrobial agent," *Water, Air, & Soil Pollution*, vol. 231, p. 130, 2020. https://doi.org/10.1007/s11270-020-04498-x

[13] Z. Moussa *et al.*, "Innovative binary sorption of Cobalt (II) and methylene blue by Sargassum latifolium using Taguchi and hybrid artificial neural network paradigms," *Scientific Reports*, vol. 12, p. 18291, 2022. https://doi.org/10.1038/s41598-022-22662-7

[14] K. N. Yogalakshmi, A. Das, G. Rani, V. Jaswal, and J. S. Randhawa, *Nano-bioremediation: A new age technology for the treatment of dyes in textile effluents. Bioremediation of Industrial Waste for Environmental Safety: Volume I: Industrial Waste and Its Management*. Singapore: Springer, 2019.

[15] A. Singh and I. Haq, *Bioremediation approaches for the removal of emerging contaminants from industrial wastewater. Current Developments in Biotechnology and Bioengineering*. Amsterdam: Elsevier, 2023.

[16] J. A. Sanjurjo-García, S. Martínez-Gallegos, P. S. Schabes-Retchkiman, and J. L. García-Rivas, "Degradation of allura red dye using Fe-Zn metal nanoparticles obtained by phytosynthesis method," *MRS Advances*, vol. 5, no. 62, pp. 3283-3291, 2020. https://doi.org/10.1557/adv.2020.392

[17] N. Nandhini, S. Rajeshkumar, and S. Mythili, "The possible mechanism of eco-friendly synthesized nanoparticles on hazardous dyes degradation," *Biocatalysis and Agricultural Biotechnology*, vol. 19, p. 101138, 2019. https://doi.org/10.1016/j.bcab.2019.101138

[18] K.-S. Chou, Y.-C. Lu, and H.-H. Lee, "Effect of alkaline ion on the mechanism and kinetics of chemical reduction of silver," *Materials Chemistry Physics*, vol. **94**, no. 2-3, pp. 429-433, 2005. https://doi.org/10.1016/j.matchemphys.2005.05.029

[19] Z. Wang, "Transmission electron microscopy of shape-controlled nanocrystals and their assemblies," *The Journal of Physical Chemistry B*, vol. 104, no. 6, pp. 1153-1175, 2000. https://doi.org/10.1021/jp993593c

[20] L. S. Devi and S. Joshi, "Antimicrobial and synergistic effects of silver nanoparticles synthesized using soil fungi of high altitudes of eastern Himalaya," *Mycobiology*, vol. 40, no. 1, pp. 27-34, 2012. https://doi.org/10.5941/MYCO.2012.40.1.027

[21] A. A. Abd El Aty, H. R. Wehaidy, and F. A. Mostafa, "Optimization of inulinase production from low cost substrates using Plackett–Burman and Taguchi methods," *Carbohydrate polymers*, vol. 102, pp. 261-268, 2014. https://doi.org/10.1016/j.carbpol.2013.11.007

[22] A. Abd Elrazak, A. C. Ward, and J. Glassey, "Polyunsaturated fatty acid production by marine bacteria," *Bioprocess Biosystems Engineering*, vol. **36**, pp. 1641-1652, 2013. https://doi.org/10.1007/s00449-013-0936-0

[23] A. Dyaa *et al.*, "Optimization of carotenoids production from Rhodotorula sp. Strain ATL72 for enhancing its biotechnological applications," *Journal of Fungi*, vol. 8, no. 2, p. 160, 2022. https://doi.org/10.3390/jof8020160

[24] H. Saleh, A. Abdelrazak, A. Elsayed, H. El-Shishtawy, and Y. Osman, "Optimizing production of a biopesticide protectant by black yeast," *Egyptian Journal of Biological Pest Control*, vol. 28, p. 72, 2018. https://doi.org/10.1186/s41938-018-0078-4

[25] A. Arya, K. Gupta, T. S. Chundawat, and D. Vaya, "Biogenic synthesis of copper and silver nanoparticles using green alga Botryococcus braunii and its antimicrobial activity," *Bioinorganic Chemistry and Applications*, vol. 2018, no. 1, p. 7879403, 2018. https://doi.org/10.1155/2018/7879403

[26] K. Ishida *et al.*, "Silver nanoparticle production by the fungus Fusarium oxysporum: Nanoparticle characterisation and analysis of antifungal activity against pathogenic yeasts," *Memórias do Instituto Oswaldo Cruz*, vol. 109, pp. 220-228, 2013. https://doi.org/10.1590/0074-0276130269

[27] S. Cheng *et al.*, "Adsorption behavior of methylene blue onto waste-derived adsorbent and exhaust gases recycling," *RSC Advances*, vol. **7**, pp. 27331-27341, 2017. https://doi.org/10.1039/C7RA01482A

[28] H. H. Lima *et al.*, "Synthesis and characterization of pecan nutshell-based adsorbent with high specific area and high methylene blue adsorption capacity," *Journal of Molecular Liquids*, vol. 276, pp. 570-576, 2019. https://doi.org/10.1016/j.molliq.2018.12.010

[29] H. A. Ahsaine, M. Zbair, Z. Anfar, Y. Naciri, N. El Alem, and M. Ezahri, "Cationic dyes adsorption onto high surface area 'almond shell'activated carbon: Kinetics, equilibrium isotherms and surface statistical modeling," *Materials Today Chemistry*, vol. **8**, pp. 121-132, 2018.

[30] H. Freundlich, "About adsorption in solutions," *Zeitschrift für physikalische Chemie*, vol. 57, no. 1, pp. 385-470, 1907. https://doi.org/10.1515/zpch-1907-5723

[31] H.-Y. Zhu, R. Jiang, L. Xiao, and W. Li, "A novel magnetically separable γ-Fe2O3/crosslinked chitosan adsorbent: Preparation, characterization and adsorption application for removal of hazardous azo dye," *Journal of Hazardous Materials*, vol. 179, no. 1-3, pp. 251-257, 2010. https://doi.org/10.1016/j.jhazmat.2010.02.087

[32] Y. Lin, Z. Chen, M. Megharaj, and R. Naidu, "Degradation of scarlet 4BS in aqueous solution using bimetallic Fe/Ni nanoparticles," *Journal of Colloid and Interface Science*, vol. 381, no. 1, pp. 30-35, 2012. https://doi.org/10.1016/j.jcis.2012.05.035

[33] C. Arab, R. El Kurdi, and D. Patra, "Efficient removal of Congo red using curcumin conjugated zinc oxide nanoparticles as new adsorbent complex," *Chemosphere*, vol. 276, p. 130158, 2021. https://doi.org/10.1016/j.chemosphere.2021.130158

[34] A. T. Mansour *et al.*, "Green synthesis of zinc oxide nanoparticles using red seaweed for the elimination of organic toxic dye from an aqueous solution," *Materials*, vol. 15, no. 15, p. 5169, 2022. https://doi.org/10.3390/ma15155169

[35] C. M. Simonescu *et al.*, "Comparative study of CoFe2O4 nanoparticles and CoFe2O4-chitosan composite for Congo red and methyl orange removal by adsorption," *Nanomaterials*, vol. 11, no. 3, p. 711, 2021. https://doi.org/10.3390/nano11030711

[36] M. A. Barakat, R. Kumar, R. F. Halawani, B. A. Al-Mur, and M. K. Seliem, "Fe3O4 nanoparticles loaded bentonite/sawdust interface for the removal of methylene blue: Insights into adsorption performance and mechanism via experiments and theoretical calculations," *Water*, vol. 14, no. 21, p. 3491, 2022. https://doi.org/10.3390/w14213491

[37] A. Kamal *et al.*, "Bioinspired green synthesis of bimetallic iron and zinc oxide nanoparticles using mushroom extract and use against Aspergillus niger; the most devastating fungi of the green world," *Catalysts*, vol. 13, no. 2, p. 400, 2023. https://doi.org/10.3390/catal13020400

[38] S. Vijayakumar, C. Krishnakumar, P. Arulmozhi, S. Mahadevan, and N. Parameswari, "Biosynthesis, characterization and antimicrobial activities of zinc oxide nanoparticles from leaf extract of Glycosmis pentaphylla (Retz.) DC," *Microbial Pathogenesis*, vol. 116, pp. 44-48, 2018. https://doi.org/10.1016/j.micpath.2018.01.003

[39] S. A. Kareem, H. M. Ahmed, O. S. Bello, and R. O. Yusuf, "Structural and optical properties of Fe_2O_3/ZnO bimetallic nanocomposites for environmental applications," *Journal of Materials Science: Materials in Electronics*, vol. 33, pp. 4567–4578, 2022.

[40] R. Khurram, Z. Wang, M. F. Ehsan, S. Peng, M. Shafiq, and B. Khan, "Synthesis and characterization of an α-Fe 2 O 3/ZnTe heterostructure for photocatalytic degradation of Congo red, methyl orange and methylene blue," *RSC Advances*, vol. 10, no. 73, pp. 44997-45007, 2020. https://doi.org/10.1039/D0RA06866G

[41] A. Labbia, B. Benhaouaa, K. Ahmoudab, Y. Meftaha, and K. Benhaouab, "Effect of iron chlorine concentration on type of green synthezed iron oxides nanoparticles using pheonixdactylifera l leaves extract," *Digest Journal of Nanomaterials & Biostructures*, vol. 16, no. 4, pp. 1627-1634, 2021.

[42] M. Vala, P. Siddhpura, P. Solanki, and B. Kataria, "Phyllanthus emblica fruit extract assisted green synthesis of ZnO nanoparticles: Thermal, vibrational, optical and electrical properties," *Materials Today: Proceedings*, vol. 76, pp. 579-584, 2023. https://doi.org/10.1016/j.matpr.2022.11.167

[43] S. S. Dappula *et al.*, "Biosynthesis of zinc oxide nanoparticles using aqueous extract of Andrographis alata: Characterization, optimization and assessment of their antibacterial, antioxidant, antidiabetic and anti-Alzheimer's properties," *Journal of Molecular Structure*, vol. 1273, p. 134264, 2023. https://doi.org/10.1016/j.molstruc.2022.134264

[44] J. Jeevanandam, A. Barhoum, Y. S. Chan, A. Dufresne, and M. K. Danquah, "Review on nanoparticles and nanostructured materials: History, sources, toxicity and regulations," *Beilstein Journal of Nanotechnology*, vol. 9, no. 1, pp. 1050-1074, 2018.

[45] M. Abbas *et al.*, "Size-controlled high magnetization CoFe2O4 nanospheres and nanocubes using rapid one-pot sonochemical technique," *Ceramics International*, vol. 40, no. 2, pp. 3269-3276, 2014. https://doi.org/10.1016/j.ceramint.2013.09.109

[46] P. Basnet and S. Chatterjee, "Structure-directing property and growth mechanism induced by capping agents in nanostructured ZnO during hydrothermal synthesis—A systematic review," *Nano-Structures & Nano-Objects*, vol. 22, p. 100426, 2020. https://doi.org/10.1016/j.nanoso.2020.100426

[47] K. Gold, B. Slay, M. Knackstedt, and A. K. Gaharwar, "Antimicrobial activity of metal and metal-oxide based nanoparticles," *Advanced Therapeutics*, vol. 1, no. 3, p. 1700033, 2018. https://doi.org/10.1002/adtp.201700033

[48] A. Sirelkhatim *et al.*, "Review on zinc oxide nanoparticles: antibacterial activity and toxicity mechanism," *Nano-Micro Letters*, vol. 7, pp. 219-242, 2015. https://doi.org/10.1007/s40820-015-0040-x

[49] J. A. Hernández-Díaz, J. J. Garza-García, A. Zamudio-Ojeda, J. M. León-Morales, J. C. López-Velázquez, and S. García-Morales, "Plant-mediated synthesis of nanoparticles and their antimicrobial activity against phytopathogens," *Journal of the Science of Food and Agriculture*, vol. 101, no. 4, pp. 1270-1287, 2021. https://doi.org/10.1002/jsfa.10767

[50] M. A. Islam, M. A. Chowdhury, M. S. I. Mozumder, and M. T. Uddin, "Langmuir adsorption kinetics in liquid media: interface reaction model," *ACS Omega*, vol. 6, no. 22, pp. 14481-14492, 2021. https://doi.org/10.1021/acsomega.1c01449

[51] J.-P. Simonin, "On the comparison of pseudo-first order and pseudo-second order rate laws in the modeling of adsorption kinetics," *Chemical Engineering Journal*, vol. 300, pp. 254-263, 2016. https://doi.org/10.1016/j.cej.2016.04.079

[52] W. S. Al-Arjan, "Zinc oxide nanoparticles and their application in adsorption of toxic dye from aqueous solution," *Polymers*, vol. 14, no. 15, p. 3086, 2022. https://doi.org/10.3390/polym14153086

[53] A. K. Prajapati and M. K. Mondal, "Comprehensive kinetic and mass transfer modeling for methylene blue dye adsorption onto CuO nanoparticles loaded on nanoporous activated carbon prepared from waste coconut shell," *Journal of Molecular Liquids*, vol. 307, p. 112949, 2020. https://doi.org/10.1016/j.molliq.2020.112949

[54] M. El-Kady, M. El-Aassar, O. A. El Batrawy, M. S. Ibrahim, H. S. Hassan, and H. Fakhry, "Equilibrium and Kinetic behaviors of cationic dye decolorization using poly (AN-co-Py)/ZrO2 novel nanopolymeric composites," *Advances in Polymer Technology*, vol. 37, no. 3, pp. 740-752, 2018. https://doi.org/10.1002/adv.21716

[55] A. Yildirim, "Kinetic, equilibrium and thermodynamic investigations for the bio-sorption of dyes onto crosslinked Pleurotus ostreatus-based bio-composite," *International Journal of Environmental Analytical Chemistry*, vol. 102, no. 17, pp. 5664-5679, 2022. https://doi.org/10.1080/03067319.2020.1802441

[56] A. B. D. Nandiyanto *et al.*, "Isotherm adsorption characteristics of carbon microparticles prepared from pineapple peel waste," *Communications in Science Technology*, vol. 5, no. 1, pp. 31-39, 2020. https://doi.org/10.21924/cst.5.1.2020.176
[57] I. Langmuir, "The adsorption of gases on plane surfaces of glass, mica and platinum," *Journal of the American Chemical society*, vol. 40, no. 9, pp. 1361-1403, 1918. https://doi.org/10.1021/ja02242a004
[58] S. Alafnan, A. Awotunde, G. Glatz, S. Adjei, I. Alrumaih, and A. Gowida, "Langmuir adsorption isotherm in unconventional resources: Applicability and limitations," *Journal of Petroleum Science and Engineering*, vol. 207, p. 109172, 2021. https://doi.org/10.1016/j.petrol.2021.109172
[59] H. A. Alalwan *et al.*, "Adsorption of methyl green stain from aqueous solutions using non-conventional adsorbent media: Isothermal kinetic and thermodynamic studies," *Bioresource Technology Reports*, vol. 14, p. 100680, 2021. https://doi.org/10.1016/j.biteb.2021.100680